Real-time characterization and source apportionment of fine particulate matter in the Delhi megacity area during late winter

Vipul Lalchandani [a], Varun Kumar [b], Anna Tobler [b], Navaneeth M. Thamban [a], Suneeti Mishra [a], Jay G. Slowik [b], Deepika Bhattu [b,1], Pragati Rai [b], Rangu Satish [c], Dilip Ganguly [d], Suresh Tiwari [e], Neeraj Rastogi [c], Shashi Tiwari [f], Griša Močnik [g], Andre S.H. Prévôt [b,*], Sachchida N. Tripathi [a,*]

[a] Department of Civil Engineering, Indian Institute of Technology Kanpur, Kanpur, India
[b] Laboratory of Atmospheric Chemistry, Paul Scherrer Institute, 5232 PSI Villigen, Switzerland
[c] Geosciences Division, Physical Research Laboratory, Ahmedabad, India
[d] Centre for Atmospheric Sciences, Indian Institute of Technology Delhi, New Delhi, India
[e] Indian Institute of Tropical Meteorology, Pune, New Delhi Branch, India
[f] Department of Civil Engineering, Manav Rachna International Institute of Research and Studies, Faridabad, Haryana, India
[g] Condensed Matter Physics Department, J. Stefan Institute, Ljubljana, Slovenia

HIGHLIGHTS

- Fine particulate matter (PM) characterization using AMS at three sites in Delhi
- Organic aerosol source apportionment using multi-linear engine (ME-2)
- Temporal trends and composition of fine PM species in Delhi megacity
- Similar PM characteristics between sites suggest similar sources of PM.

GRAPHICAL ABSTRACT

Fine particulate matter characterization and organic aerosol sources in Delhi megacity
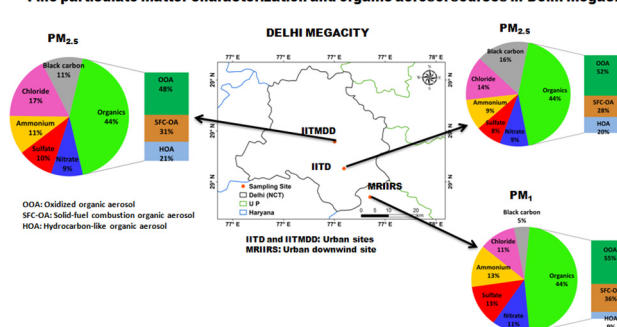
ARTICLE INFO

ABSTRACT

National Capital Region (NCR) encompassing New Delhi is one of the most polluted urban metropolitan areas in the world. Real-time chemical characterization of fine particulate matter (PM$_1$ and PM$_{2.5}$) was carried out using three aerosol mass spectrometers, two aethalometers, and one single particle soot photometer (SP2) at two sites in Delhi (urban) and one site located ~40 km downwind of Delhi, during January–March 2018. The campaign mean PM$_{2.5}$ (NR-PM$_{2.5}$ + BC) concentrations at the two urban sites were 153.8 ± 109.4 µg.m^{-3} and 127.8 ± 83.2 µg.m^{-3}, respectively, whereas PM$_1$ (NR-PM$_1$ + BC) was 72.3 ± 44.0 µg.m^{-3} at the downwind site. PM$_{2.5}$ particles were composed mostly of organics (43–44)% followed by chloride (14–17)%, ammonium (9–11)%, nitrate (9%), sulfate (8–10)%, and black carbon (11–16)%, whereas PM$_1$ particles were composed of 47% organics, 13% sulfate as well as ammonium, 11% nitrate as well as chloride, and 5% black carbon. Organic aerosol (OA) source apportionment was done using positive matrix factorization (PMF), solved using an advanced multi-linear engine (ME-2) model. Highly mass-resolved OA mass spectra at one urban and downwind site were factorized into three primary organic aerosol (POA) factors including one traffic-related and two solid-fuel combustion (SFC), and three oxidized OA (OOA) factors. Whereas unit mass resolution OA at the other urban site was factorized into two POA factors related to traffic and SFC, and one OOA factor. OOA constituted a majority of the total OA mass (45–55)% with maximum contribution during afternoon hours ~(70–80)%. Significant

differences in the absolute OOA concentration between the two urban sites indicated the influence of local emissions on the oxidized OA formation. Similar PM chemical composition, diurnal and temporal variations at the three sites suggest similar type of sources affecting the particulate pollution in Delhi and adjoining cities, but variability in mass concentration suggest more local influence than regional.

1. Introduction

Fine particulate matter adversely affects human health (Pope and Dockery, 2006), local and regional climate (Seinfeld and Pankow, 2003), and causes 4.2 million deaths globally every year (World Health Organisation, 2018). The National Capital Region (NCR), one of the world's largest urban agglomerations includes India's capital (New Delhi) along with districts (Gurugram, Faridabad, and Noida) from the adjoining states of Haryana and Uttar Pradesh. New Delhi was found to be the most polluted city in the world, with an annual mean $PM_{2.5}$ concentration of ~140 $\mu g.m^{-3}$ (World Health Organisation, 2018). The global annual population-weighted $PM_{2.5}$ was estimated to be ~46 $\mu g.m^{-3}$, while ~91 $\mu g.m^{-3}$ for India in 2017 (Cohen et al., 2017).

Aerosols affect the solar radiation budget by directly absorbing and scattering sunlight, and indirectly by acting as cloud condensation nuclei (Albrecht, 1989; TWOMEY et al., 1984). Quantification of the source-aerosol relationship is crucial for predicting the climate effects of aerosols. Predominantly, organic aerosol (OA) constitutes a major fraction (20–90%) of sub-micron aerosol mass (Jimenez et al., 2009; Zhang et al., 2007). OA is classified as either primary organic aerosol (POA), which is emitted directly in the atmosphere, and often but not always related to combustion activities. OA is emitted from both anthropogenic sources such as vehicles, industrial and cooking, and natural sources such as forest fires, or secondary organic aerosol (SOA), which is formed in the atmosphere from the oxidation of precursor gases such as volatile organic compounds (VOCs) (Kanakidou et al., 2005; Fuzzi et al., 2006; Hallquist et al., 2009; Han et al., 2016). Understanding the sources and formation pathways of OA is a challenging task as it is composed of thousands of compounds, many of which are unknown, which continuously evolve in the atmosphere (Jimenez et al., 2009).

Highly time-resolved real-time monitoring of non-refractory (NR) PM chemical species can be done using time-of-flight aerosol chemical speciation monitor (ToF-ACSM) (Fröhlich et al., 2013), and high-resolution time-of-flight aerosol mass spectrometer (HR-ToF-AMS) (Canagaratna et al., 2007; Jayne et al., 2000), which measures size-resolved mass spectra as well. The detailed working of different types of AMS developed, and its applications in various field experiments can be found in Canagaratna et al. (2007).

OA mass spectra can be used in bilinear factorization receptor models such as positive matrix factorization (PMF) for apportioning the total OA into factors representing different sources and/or atmospheric processes (Lanz et al., 2007; Ulbrich et al., 2009). Multiple studies have used AMS data for investigating OA sources in both rural and urban environments in India (Chakraborty et al., 2015; Chakraborty et al., 2017; Kumar et al., 2016; Thamban et al., 2017) and across the world (Jimenez et al., 2009; Lanz et al., 2010; Ng et al., 2010; Zhang et al., 2007, 2011). However, PMF source apportionment is often not able to resolve the sources with similar temporal variation and/or profiles. Advanced source apportionment method such as multi-linear engine (ME-2) (Paatero, 1999) has been used for apportioning OA sources by constraining one or more known factor profiles or time series resulting in a clean separation of primary and secondary sources, which is otherwise not possible through conventional PMF model (Canonaco et al., 2013; Crippa et al., 2014; Lanz et al., 2008).

Most of the previous studies in Delhi-NCR have used low time resolution filter-based methods for characterization and source apportionment of fine and coarse PM (Nagar et al., 2017; Pant et al., 2015; Sharma et al., 2016; Singhai et al., 2017), which are unable to

capture the temporal trend in concentration, and suffer from sampling artifacts. In other parts of India, only a handful of studies have been done on real-time PM characterization and source apportionment using AMS (Chakraborty et al., 2015; Mukherjee et al., 2018). Gani et al. (2019) was the first study in Delhi reporting real-time temporal and seasonal variation of PM_1 and its species, using Quadrupole-ACSM (Q-ACSM) data at the Indian Institute of Technology Delhi (IITD), New Delhi from January 2017 to April 2018 (one of the sites of this study), and found more than 50% organic content with the highest concentration observed during the winter season (mean PM_1 = ~210 $\mu g.m^{-3}$). Tobler et al. (2020) carried out the $PM_{2.5}$ characterization and OA source apportionment using highly time-resolved ToF-ACSM measurements and found (39–49)% OA in $PM_{2.5}$ from December 2017 to May 2018. A part of the long-term data analyzed in that study has been used here (February–March). The present study is the second continuous measurement of NR-PM species in Delhi, and the first multi-site measurement in Delhi-NCR to study local and temporal differences in fine particulate matter concentration. The objective of this study is to characterize the real-time fine particulate matter, explore the temporal and diurnal variation of the constituent species, and investigate OA sources and/or evolution pathways using positive matrix factorization.

Here, we investigate the composition and sources of PM in the New Delhi area via highly time-resolved measurements at three sites. NR-$PM_{2.5}$ was measured at two sites in New Delhi while NR-PM_1 was measured at an urban downwind site in Faridabad, Haryana using AMS. Real-time black carbon (BC) mass concentrations were also measured at all sites. Further, the ME-2 algorithm was used for source apportionment of OA mass spectra from AMS at the three sites.

2. Methods

2.1. Sampling site description

Delhi-NCR includes the National Capital Territory of Delhi and districts from adjoining states of Uttar Pradesh, Haryana, and Rajasthan. This encompasses approximately 58,000 km^2 and a population of over 47 million. NCR has a semi-arid climate and is surrounded by the Thar Desert on the west and the Indo-Gangetic plains to the south-east. It experiences hot and dry summer (April to June) with temperatures ranging from ~20 °C to ~48 °C, and cold and humid winter (December to February) with temperature ranging from ~2 °C to ~15 °C. It experiences north-westerly winds during most of the year except during the monsoon season (southern winds; July to mid-September). Sampling was conducted at two sites in New Delhi: Indian Institute of Technology Delhi (IITD) (28.54° N, 77.19° E) and Indian Institute of Tropical Meteorology Delhi (28.62° N, 77.17° E), hereafter referred to as IITD and IITMDD, respectively, and a downwind site located ~40 km north-west to New Delhi in Faridabad, Haryana: Manav Rachna International Institute of Research and Studies (MRIIRS) (28.45° N, 77.28° E) during January–March 2018. IITMDD is a central urban part of Delhi, surrounded by forest area and residential colonies. On the other hand, IITD is more of an urban residential site surrounded by moderate traffic density roads (~200 m away). Further, MRIIRS is an educational institute and is located close to the main road with both heavy and light-duty vehicles. The hourly averaged temperature observed during the sampling period ranged from ~8 °C to ~36 °C with an average value of 19.1 ± 6.2 °C at the IITD site and 20.8 ± 5.7 °C at the MRIIRS site.

While average relative humidity observed at IITD was 54.3 ± 23.7% (8.1–99.1) and 53.8 ± 19.0% (15.6–99.5) at MRIIRS.

2.2. Sampling details and instrumentation

At the IITD site, a high-resolution long-time-of-flight aerosol mass spectrometer (L-ToF-AMS), equipped with $PM_{2.5}$ aerodynamic lens (Peck et al., 2016) (Aerodyne Research Inc., Billerica, MA, USA), and a seven wavelength aethalometer model AE-33 (Aerosol d.o.o., Ljubljana, Slovenia) (Drinovec et al., 2015) were installed inside a temperature-controlled laboratory on the 3rd floor of Centre for Atmospheric Science (CAS) building located at a height of ~10 m above ground. Ambient aerosols were sampled through $PM_{2.5}$ cyclone (BGI, Mesa Labs. Inc.) inlet located ~2 m above the rooftop using ~3 m long stainless steel tubing (6 mm I.D.; 8 mm O.D.). The particles were dried using an aerosol sample dryer system (Aerodyne research, Inc) to achieve output RH of ~20%. The ambient aerosol data were collected from 17th January, 2018 - 19th January, 2018 & 5th February, 2018 – 11th March, 2018. The data between 19th January to 5th February was not available, as the AMS was not operated during this period due to hardware issues.

At the IITMDD site, a time-of-flight aerosol chemical speciation monitor (ToF-ACSM) (Aerodyne Research Inc., Billerica, MA, USA) (Fröhlich et al., 2013), equipped with $PM_{2.5}$ aerodynamic lens (Peck et al., 2016), and a seven wavelength aethalometer (model AE-33) were installed inside a temperature-controlled laboratory on the second floor of the main building at a height of ~8 m from the ground. Ambient aerosols were sampled through a $PM_{2.5}$ cyclone (BGI, Mesa Labs, Inc.) placed on the roof (~1.5 m above the rooftop) at 5 L.min^{-1} and transmitted through stainless steel tubing (12 mm O.D.). A bypass flow of 1.9 L. min^{-1} was maintained using an external pump to achieve the required flow of $PM_{2.5}$ cyclone. A Nafion dryer (MD-110-48S-4) was installed after bypass to dry the ambient aerosol. The dried aerosol flow was split between ACSM and aethalometer which sampled at 0.1 L.min^{-1} and 3 L.min^{-1}, respectively. The ambient aerosol data were collected from December 2017 to May 2018, however, only a portion of the whole data (17th February-15th March, 2018), which coincides with the AMS data from IITD and IITMDD sites, has been discussed here. The overall data has been discussed in our companion paper (Tobler et al., 2020).

At MRIIRS site, a high-resolution time-of-flight aerosol mass spectrometer (HR-ToF-AMS, Aerodyne Research Inc., Billerica, MA) (Canagaratna et al., 2007; DeCarlo et al., 2006) along with a scanning mobility particle sizer (SMPS, TSI.inc), equipped with PM_1 aerodynamic lens, and Droplet Measurement Technologies (DMT) Single Particle Soot Photometer (SP2), was installed inside a temperature-controlled laboratory on the first floor at a height of ~4 m above ground. Aerosols were pumped in using ~1.5 m long and 0.19 inch inner diameter (TSI. inc) silicon tubing through a window, after which it was dried using a silica diffusion dryer which was regenerated frequently to maintain RH of ~20%. The dried aerosol was split between AMS and SMPS sampling at 0.08 L.min^{-1} and 0.3 L.min^{-1}, respectively. SP2 was connected directly to the ambient air as it can operate between 0 and 100% RH similar to the setup described elsewhere (Laborde et al., 2013; Liu et al., 2013; Shamjad et al., 2016). The ambient aerosol data were collected from 27th January, 2018 to 15th March, 2018.

2.2.1. Aerosol mass spectrometers

NR-PM is operationally defined as the PM components that vaporize at 600 °C and ~10^{-5} Torr. These typically include organics, nitrate, sulfate, ammonium, and some chlorides, but exclude black carbon, sea salt, mineral dust, and metals.

HR-ToF-AMS measures size-resolved mass spectra of NR component of either PM_1 or $PM_{2.5}$ (respectively denoted as NR-PM_1 and NR-$PM_{2.5}$), depending on the installed inlet and aerodynamic lens. The detailed working of HR-ToF-AMS has been described in DeCarlo et al. (2006).

Briefly, aerosol particles are sampled through a 100 μm diameter critical orifice and enter the aerodynamic lens system where it is focused into a narrow beam. A combination of inlet and aerodynamic lens system efficiently transmits particles smaller than 1 or 2.5 μm vacuum aerodynamic diameter (transmission efficiency 100% for $D_{aero} = 35$ nm to 700 nm for PM_1 and more than 50% for $PM_{2.5}$ particles) (DeCarlo et al., 2006; Peck et al., 2016). The focused particle beam enters the sizing chamber where the particle size is determined by measuring the time it takes to travel the fixed length of the sizing chamber. The particle beam then impacts the vaporizer heated at 600 °C (at 10^{-7} Torr) which evaporates the non-refractory particles. The resulting gas molecules are ionized by electron ionization at 70 eV, and the ions formed are detected by a time-of-flight mass spectrometer according to their mass to charge ratio (m/z). HR-ToF-AMS was operated in V-mode which offers high sensitivity but lower resolution, with a sampling time of 2 min during which it alternated between mass spectra (MS) and particle time-of-flight (PToF) mode every 30 s completing 2 cycles. During MS mode, mass spectra of an ensemble of particles are measured whereas in PToF mode particle beam is modulated by a chopper rotating at ~130 Hz, thus measuring size-resolved mass spectra. In MS mode, it switched between open and closed mode every 15 s measuring particle plus gas and particle-free gas, respectively. Unit mass resolution (UMR) data were analyzed using the SQUIRREL data analysis toolkit (version 1.59) programmed in IGOR Pro 6.37 software (Wavemetrics, Inc., Portland, OR, USA). High-resolution data were analyzed using PIKA (version 1.19) following peak fitting algorithm (DeCarlo et al., 2006) for m/z 12 to 120 for both sites. Particle free air measurements were performed every week for 1–2 h using a HEPA filter to correct the standard fragmentation table at m/z's 12, 16, 18, 29, 33, 34, 40, 44 in case of HR-ToF-AMS, and at m/z's 16, 18 and 44 in case of L-ToF-AMS, for the air interferences (Aiken et al., 2008; Allan et al., 2004). AMS NR-PM_1 mass concentration at the MRIIRS site was compared with PM_1 mass estimated from SMPS measured volume concentration by assuming a density of 1.4 g.cm^{-3}, as the effective density of ambient particles in Asia, was estimated to range between 1.3 and 1.6 g.cm^{-3} (Sarangi et al., 2016; Hu et al., 2012; Thamban et al., 2019).

L-ToF-AMS has the same operation and principle as HR-ToF-AMS but has a mass spectrometer with approximately two times the length of the mass spectrometer in HR-ToF-AMS offering twice the mass resolution as HR-ToF-AMS in V-mode. L-ToF-AMS sampled at a flow rate of ~0.08 lpm with an averaging time of 2 min and alternated between MS (30 s open and 30 s closed position) and PToF mode every 1 min.

The ToF-ACSM has the same working principle as AMS except it does not measure the size of the particles. A detailed description of the ToF-ACSM can be found in Fröhlich et al. (2013). An ACSM measures ambient air and particle-free air, generated using a particle filter in the sampling line, alternatively every 20 s, and the difference of the two mass spectra represents the particle mass spectra. The mass spectra of 20 cycles were integrated resulting in a time resolution of 10 min. The raw data were analyzed using Tofware 2.5.13. Further details of sampling, instrument operation and data analysis can be found in our companion paper (Tobler et al., 2020).

Composition-dependent collection efficiency (CDCE) was calculated according to the method of Middlebrook et al. (2012). For IITD AMS, a time-dependent CDCE correction was applied to AMS measured species (average collection efficiency (CE) = 0.5 ± 0.01), whereas, for MRIIRS, a CE of 0.5 ± 0.01 was calculated and applied to the AMS measured mass concentrations. AMS measured NR-PM_1 mass correlated strongly with SMPS measured PM_1 mass at MRIIRS with R^2 value of 0.84 and a slope of 0.80 (Fig. S1). A CE of 0.5 was assumed for ToF-ACSM, as no sufficiently acidic particles were found to affect the calculations and ammonium nitrate mass fraction was less than 40% in more than 99% of the data.

Ionization efficiency calibrations were performed at the beginning of the campaign by injecting mono-disperse 300 nm ammonium nitrate and ammonium sulfate particles into AMS/ACSM and a condensation

particle counter (Jayne et al., 2000). For AMS, a relative ionization efficiency value of 3.89 and 4.1 were calculated for NH_4^+ for IITD and MRIIRS, respectively, while a standard RIE of 1.4, 1.3, and 1.2 were assumed for organics, chloride, and sulfate, respectively. For ACSM data, RIE of 2.83 and 1.06 for ammonium and sulfate, respectively, were determined experimentally, whereas standard RIE of 1.4 was assumed for organics and chloride.

2.2.2. Supporting measurements

Aethalometer (Magee Scientific, model AE-33) was deployed at IITD and IITMDD sites to measure real-time black carbon (BC) mass concentrations. It measures the light attenuation of particles collected on a quartz fiber filter at 7 wavelengths (370, 470, 520, 590, 660, 880, and 950 nm) which is then used to calculate the aerosol absorption coefficient (b_{abs}) as per Beer-Lambert's law:

$$I = I_0 . e^{-b_{abs} . x} \tag{1}$$

where I_0 is the intensity of light falling on the particle-laden filter, I is the intensity of light passing the filter, and x is the thickness of the filter. BC concentration was calculated from b_{abs} at 880 nm using a mass absorption cross-section (MAC) of 7.77 $m^2.gm^{-1}$. The AE33 aethalometer corrects for loading effects in real-time using the dual spot technique (Drinovec et al., 2015, 2017). However, IITM data was post-processed for loading effect correction as the instrument correction failed for high mass loading, details of which can be found elsewhere (Tobler et al., 2020).

At MRIIRS, SP2 was used to measure real-time BC mass concentration in the size range of 70–500 nm. SP2 uses an intracavity Nd:YAG laser beam to intercept the aerosol flow in a perpendicular plane, and heats individual BC particles to their vaporization temperature. As a result, BC particle emits incandescent light which is detected using avalanche photodiodes, and is used to estimate BC mass. A detailed description of the principle and working of SP2 can be found elsewhere (Gao et al., 2007; Moteki and Kondo, 2007, 2010; Schwarz et al., 2006; Stephens et al., 2003; Subramanian et al., 2010; Wang et al., 2014). In the present study, SP2 was operated at a flow rate of 30 cubic centimeters per minute (ccm) and calibrated with Aquadag following the standard protocol as described in Thamban et al. (2017). Data were analyzed using standard SP2 software version 4.3.3. Additionally, Scanning Mobility Particle Sizer (SMPS, TSI.Inc) was deployed at all three sites to obtain PM_1 mass concentration. The meteorological parameters (temperature and relative humidity) were measured at IITD and MRIIRS using an automatic weather station (AWS).

2.3. Source apportionment

2.3.1. OA source apportionment

Source apportionment of OA mass spectra was performed using the PMF model (Paatero and Tapper, 1994) for all sites. The ME-2 algorithm (Paatero, 1999) was used to solve the PMF model and was controlled via the Source Finder (SoFi, Datalystica Ltd., Villigen, Switzerland) (Canonaco et al., 2013) interface version 6.6.

PMF is a receptor model for solving bilinear unmixing equation where a measured quantity (in the present study the organic mass spectral time series) can be factorized into a linear combination of a number of constant factor profiles and their corresponding time series as per the following equation:

$$x_{ij} = \sum_{k=1}^{p} \left(g_{ik} . f_{kj} \right) + e_{ij} \tag{2}$$

where, i, j, and k represent a timestamp, a measured variable, and a particular factor, respectively. x_{ij}, g_{ik}, f_{kj} and e_{ij} are elements of the measured organic matrix, time series of factor contributions, factor profiles, and residual matrix, respectively. The model uses a least square algorithm

to iteratively minimize the fit parameter Q, which is defined as the sum of the squares of the ratio of residual (e_{ij}) to measurement uncertainties (σ_{ij}).

$$Q = \sum_{i=1}^{m} \sum_{j=1}^{n} \left(\frac{e_{ij}}{\sigma_{ij}} \right)^2 \tag{3}$$

where m is the number of samples (time series) and n is the number of variables (ions or m/z) in the matrix. PMF does not require a priori information of the source profile or their temporal contribution. However, PMF can result in mathematically accurate but not unique solutions through several linear combinations of the factor profile and time series, also known as rotations (Paatero and Hopke, 2009; Ulbrich et al., 2009). As a result, mixed factor profiles and inaccurate factor attribution are possible (Canonaco et al., 2013, 2015; Crippa et al., 2014). In ME-2, these rotations can be efficiently explored by constraining one or more elements of factor profile and/or time series in the PMF model using known information of source profile (s) and/or temporal variation as a priori information, referred to as a-value approach. The a-value represents the degree of constraint on the known source profile and/or time series, and varies from zero to one with zero being fully constrained (Lanz et al., 2008). Here, we have used the a-value approach for the IITMDD and MRIIRS PMF solutions.

For the IITD site, OA mass spectra obtained from HR analysis of m/z 12 to 120 (320 ions) was combined with UMR OA mass spectra from m/z 121 to 350 (225 ions), resulting in a combined PMF input matrix containing 545 ions/variables. Similarly, for the MRIIRS site, HR ions from m/z 12 to 120 (369 ions) were combined with UMR (m/z 121 to 300; 176 ions), resulting in a combined PMF input matrix containing 445 variables. Variables with a signal-to-noise ratio < 0.2 were down-weighted by a factor of 10 whereas those with SNR <2 were down-weighted by a factor of 2 (Paatero and Hopke, 2003). Further, CO_2^+ related variables (O^+, OH^+, $H_2O^{+\cdot}$ and CO^+) were excluded from PMF analysis to avoid overweighting CO_2^+ intensity. The variables were added to the OA spectra post-PMF analysis. The final input matrix contained 541 ions and 4452 data points (10 min averaged) for the IITD site, and 441 ions and 3960 data points for MRIIRS (15 min averaged). For the IITMDD site, OA mass spectra included 177 ions ranging from 12 to 210. The CO_2^+-related ions were added to the OA mass spectra post-PMF analysis. The PMF results for the IITMDD site were taken from our companion paper (Tobler et al., 2020), in which PMF was run on OA data from 17th February to 27th April, 2018. Here, we have taken the factors time series from 17th February to 15th March, 2018, coinciding with the AMS data from IITD and MRIIRS, as mentioned previously in Section 2.2.

2.3.2. BC source apportionment

The multi-wavelength BC data from Aethalometer can be apportioned into biomass burning and traffic combustion sources utilizing enhanced absorption of biomass burning aerosols in near ultra-violet and blue wavelength range, as compared to fossil fuel sources such as traffic (Sandradewi et al., 2008; Zotter et al., 2017). The model assumes that light-absorbing particles originate only from traffic and biomass burning sources, and uses absorption Ångström exponent (AAE) value corresponding to traffic and biomass burning sources. According to past studies, traffic AAE values fall in the range of (0.8–1.1), whereas (0.9–3.5) for biomass burning emissions (Kirchstetter et al., 2004; Lewis et al., 2008; Saleh et al., 2013; Schnaiter et al., 2003, 2005). In the present study, AAE values of 0.9 for traffic and 1.5 for biomass burning emissions are taken from our companion paper (Tobler et al., 2020).

2.4. Backward trajectory (BT) clustering and concentration weighted trajectory (CWT)

To understand the origin of air masses and their travel path, a BT analysis was performed using HYSPLIT (v4.1, Hybrid Single-Particle

Lagrangian Integrated Trajectory) (Draxler et al., 2018; Stein et al., 2015) model using a Weekly GDAS (Global Data Assimilation System) files (ftp://arlftp.arlhq.noaa.gov/pub/archives/gdas1) with a 1° × 1° resolution. The BT were calculated every 3-h for an arrival height of 100 m above ground level (a.g.l) so that they ended within the mixing layer. The calculated BT were weighed with OA factors time series, using a CWT model to localize air parcels responsible for high concentrations at the receptor site. OA factors time series were averaged to 3-h to match the BT time resolution, and CWT were calculated using Igor-based user interface, ZeFir (Petit et al., 2017), according to the following equation

$$CWT_{ij} = \frac{1}{\tau_{ij}} \sum_{k=1}^{N} C_k \tau_{ijk} \qquad (4)$$

where, i, j represents the latitude and longitude; CWT_{ij} (μg m^{-3}) is the average weighted trajectory concentration in the ijth cell; k is the index of the trajectory, N is the total number of trajectories, C_k (μg m^{-3}) is the measured factor concentration of trajectory k; and τ_{ijk} is the residence time of trajectory k in the ijth cell.

3. Results and discussion

3.1. PM species concentration and temporal variation

Fig. 1 shows the temporal variation of hourly averaged mass concentration of total PM$_{2.5}$ (IITD and IITMDD) and PM$_1$ (MRIIRS) and its constituent species for the campaign period. The sum of NR-PM and BC is represented here as equivalent PM concentration written hereafter as PM (eq.), however, it is important to note that it does not include refractory elements like metals.

Similar temporal trends were observed between the three sites for total PM and individual species mass concentrations. Highest PM loadings were observed at IITD with campaign hourly average PM$_{2.5}$ (eq.) (NR-PM$_{2.5}$ + BC) concentration of 153.8 ± 109.4 μg.m^{-3}, and maximum concentration reaching up to 596.2 μg.m^{-3} (observed during the night at 10 pm), followed by IITMDD at 127.8 ± 83.2 μg.m^{-3} with maximum concentration reaching up to 391.3 μg.m^{-3} (observed during the morning at 9 am). Whereas, hourly average PM$_1$ (eq.) concentration at MRIIRS was 72.3 ± 44.0 μg.m^{-3}, with a maximum concentration of 250 μg.m^{-3} (observed during late night at 1 am). Similarly, the highest NR-PM$_{2.5}$ concentration was observed at IITD with an hourly average value of 125.2 ± 93.3 μg.m^{-3}, ranging from 6.4 to 484.9 μg.m^{-3},

followed by IITMDD with an hourly average concentration of 114.5 ± 81.4 μg.m^{-3}, ranging from 14.6 to 356.4 μg.m^{-3}. Hourly average NR-PM$_1$ concentration at MRIIRS was 65.9 ± 41.7 μg.m^{-3}, ranging from 7.1 to 239.3 μg.m^{-3}. The percent contribution of NR-PM in PM (eq.) was 81%, 89%, and 91% for IITD, IITMDD, and MRIIRS, respectively. Daily average PM$_{2.5}$ (eq.) loading at IITD site (146.2 ± 76.4 μg.m^{-3}) was ~2.4 times higher than NAAQS (60 μg.m^{-3}) and ~ 6 times higher than WHO daily average PM$_{2.5}$ standard (25 μg.m^{-3}), however, for IITMDD, it was ~2 and ~ 5 times higher, respectively. Very high chloride concentrations were observed at all sites, with campaign mean concentrations of 20.4 ± 30.3 μg.m^{-3}, 22.3 ± 27.6 μg.m^{-3} and 7.7 ± 9.7 μg.m^{-3}, and maximum concentrations of 209.5 μg.m^{-3}, 126.4 μg.m^{-3} and 68.2 μg.m^{-3} at IITD, IITMDD and MRU, respectively. Gani et al. (2019) has also reported multiple episodes of chloride concentrations exceeding 100 μg.m^{-3}, measured using ACSM at the IITD site, during the winter of 2017. Several other studies have also reported high particulate chloride concentrations in Delhi (mainly in the form of NH$_4$Cl) in the winter season because of low temperature, high RH, and less vertical mixing (Rai et al., 2020; Bhandari et al., 2020; Gani et al., 2019; Pant et al., 2015). Pant et al. (2015) identified coal combustion, biomass burning, and waste burning as the probable source of chloride, using molecular markers for source identification. Patil et al. (2013) developed source profiles of 27 sources in six Indian metropolitan cities including New Delhi, and found an abundance of chloride in several sources such as wood and coal combustion, agriculture waste burning, garden waste burning, Bagasse combustion and open solid waste burning (paper, plastic and packing materials). Using real-time measurement and source apportionment of elements in Delhi during the 2018 and 2019 winter period, Rai et al. (2020) suggested chlorine likely to be emitted from numerous brick kilns using coal and biomass burning for baking bricks, and steel industries using HCl in the pickling process of hot and cold steel sheets.

For the whole campaign period, average, standard deviation, maximum, and minimum concentration values of NR-PM, organic, nitrate, sulfate, ammonium, chloride, and PM (eq.) are listed in Table 1. PM (eq.) is calculated for the period where both BC and NR-PM species concentrations were available. Similar average NR-PM$_{2.5}$ levels were observed at IITD and IITMDD, but were around ~(1.7–1.9) times that of NR-PM$_1$ at the MRIIRS site, respectively. The AMS at MRIIRS sampled PM$_1$ particles unlike IITD and IITMDD sites; therefore, direct comparison of absolute concentration levels between MRIIRS and the other two sites cannot be done. The campaign average BC concentration was highest at IITD (24.5 ± 20.6 μg.m^{-3}) followed by IITMDD (14.4 ± 9.9 μg.m^{-3}), while significantly lower levels were observed at MRIIRS (3.3 ±
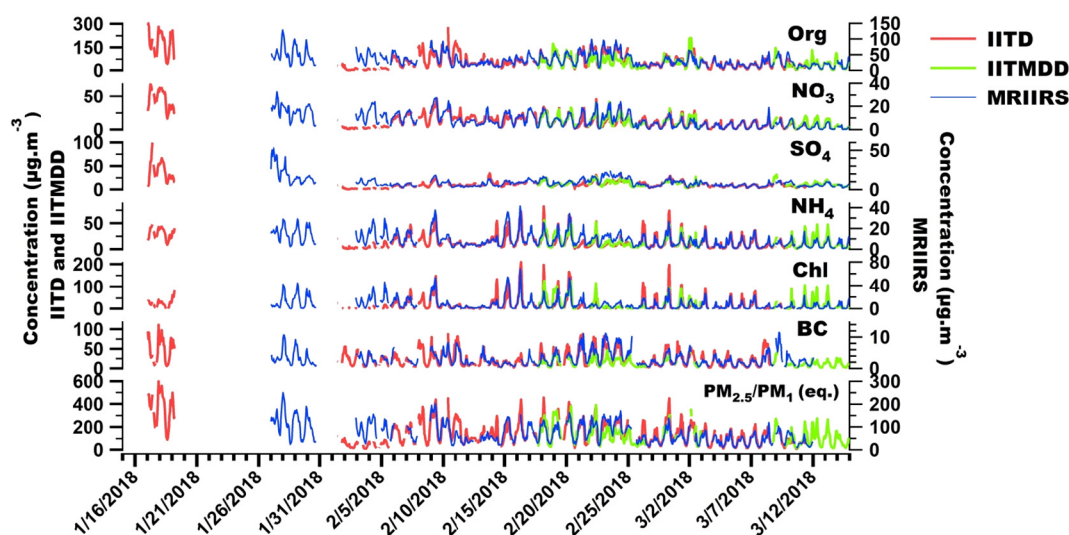

Fig. 1. Temporal variation of mass concentration (μgm^{-3}) of PM$_{2.5}$ species at IITD (L-ToF-AMS) and IITMDD (ToF-ACSM), and PM$_1$ at MRIIRSS (HR-ToF-AMS) site. PM (eq.) represents the sum of NR-PM and BC.

Table 1

Average, standard deviation, maximum and minimum mass concentrations of PM species for the campaign period (organics (Org), nitrate (NO_3), sulfate (SO_4), ammonium (NH_4), chloride (Chl) and black carbon (BC)) for IITD, IITMDD and MRIIRS. For IITD and IITMDD all parameters represent $PM_{2.5}$ component whereas PM_1 for MRIIRS.

	Mean ± Std ($\mu g.m^{-3}$)			Max ($\mu g.m^{-3}$)			Min ($\mu g.m^{-3}$)		
	IITD	IITMDD	MRIIRS	IITD	IITMDD	MRIIRS	IITD	IITMDD	MRIIRS
Org	65.3 ± 51.68	55.0 ± 37.4	32.4 ± 20.5	304.1	211.4	128.5	3.4	4.4	3.5
NO_3	13.3 ± 12.1	11.1 ± 8.0	8.0 ± 6.2	68.2	41.3	32.8	0.4	0.7	0.2
SO_4	12.0 ± 10.1	12.5 ± 5.3	8.9 ± 6.2	99.9	32.0	53.2	0.6	2.8	2.0
NH_4	14.3 ± 13.5	13.6 ± 11.4	9.0 ± 6.9	82.5	55.8	41.4	0.6	1.6	0.6
Chl	20.4 ± 30.3	22.3 ± 27.6	7.7 ± 10.0	209.5	126.4	68.2	0.1	0.2	0.1
BC	24.5 ± 20.6	14.4 ± 9.9	3.3 ± 2.4	111.3	46.4	17.6	1.4	1.6	0.4
NR-PM	125.2 ± 93.3	114.5 ± 81.4	65.9 ± 41.7	484.9	356.4	239.3	6.4	14.6	7.1
PM (eq.)	153.8 ± 109.4	127.8 ± 83.2	72.3 ± 44.0	596.2	391.3	250.0	12.8	16.4	9.0

2.4 $\mu g.m^{-3}$), indicating the IITD site to be most affected by combustion-related emissions such as traffic and burning of solid fuels. Lower concentration levels at MRIIRS than IITD and IITMDD were also probably because it is located downwind of Delhi and the emissions are expected to be diluted and less trapped. Similarly, significantly higher mixing ratios of volatile organic compounds (VOCs), measured using proton-transfer-reaction time-of-flight mass spectrometers (PTR-ToF-MS), were observed at IITD (27.6 ppbv), as compared to MRIIRS (19.4 ppbv) during the same measurement period (Wang et al., 2020).

Campaign average concentrations (overall and separated by day and night hours) of PM_1/$PM_{2.5}$ species and their percent contribution to total PM at three sites are shown in Fig. 2(a & b). On average, $PM_{2.5}$ particles at IITD and IITMDD were composed of ~(43–44)% organics, ~(14–17)% chloride, ~(9–11)% ammonium, ~9% nitrate, ~(8–10)% sulfate, and ~(11–16)% BC, whereas at MRIIRS PM_1 particles were composed of 47% organics, 13% sulfate as well as ammonium, 11% nitrate as well as chloride, and 5% BC. During the winter of 2017, Gani et al. (2019) found a relatively higher contribution of organics (53%), whereas, lower contribution of BC (7%) and chloride (11%) in PM_1

using Q-ACSM at IITD, however, relatively similar contribution of nitrate, sulfate, ammonium, and sulfate (8–11) % were found. The dominance of organics fraction in PM fine fraction is consistent with earlier studies in India (Chakraborty et al., 2015; Kumar et al., 2016) and across the world (Jimenez et al., 2009; Zhang et al., 2007). Crippa et al. (2013a) also found similar PM_1 composition using AMS during January–February 2010, between urban and urban background sites in the metropolitan area of Paris, indicating the influence of regional sources on air quality. However, much lower average NR-PM_1 levels (average ~14–18 $\mu g.m^{-3}$) were observed, as compared to the present study, with average NR-PM_1 at MRIIRS being ~66 $\mu g.m^{-3}$ while NR-$PM_{2.5}$ at IITMDD and IITD being ~114 $\mu g.m^{-3}$ and ~196 $\mu g.m^{-3}$, respectively.

Similar PM composition and temporal variation were observed between the three sites except for lower BC fraction in PM_1 at MRIIRS, which may suggest that the particle pollution at the three sites was majorly influenced by similar sources. It should be noted that the BC at MRIIRS was measured using SP2 which detects BC particles in the size range of 70–500 nm. Differences in PM chemical composition during day and night were examined by separating the overall data in day
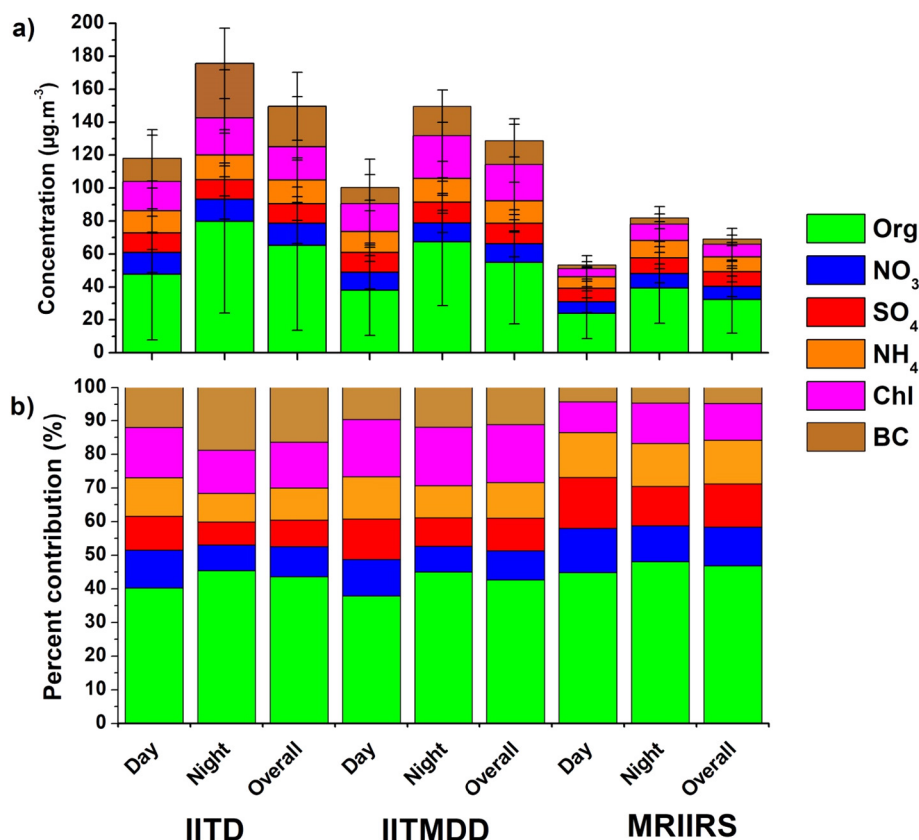

Fig. 2. Average absolute concentration of PM species (a), and average percent contribution to total PM (b), separated by day, night and overall, at IITD, IITMDD, and MRIIRS sites.

(7 am to 6 pm) and night hours (6 pm to 7 am). At all three sites, higher inorganics contribution to total PM concentration was observed during the day (48–52%) than night (36–48%), whereas organics and BC contribution was higher during the night (46–48% and 5–19%) than day (38–45% and 4–12%) (Fig. 2). A higher contribution of inorganics during the day can be attributed to an increase in the formation of semi-volatile species such as nitrate, ammonium, and chloride by gas to particle conversion during night time, when the temperature was low and RH was high (Fig. S2). The overnight formation and accumulation of secondary semi-volatile species resulted in the high morning peak (~6–9 AM) (Fig. 3) coinciding with the lowest temperature and highest RH values of the day (Fig. S2). Similar high morning time concentrations of nitrate and chloride were also observed by Gani et al. (2019) during the winter months in New Delhi. Whereas, higher contribution of organics and BC during night could be attributed to a combination of stagnant conditions at night owing to reduced planetary boundary layer and, increase in solid fuel combustion activities and traffic emissions during peak evening traffic hours as evident in Fig. 3.

PM species exhibited strong and similar diurnal variations at all three sites as shown in Fig. 3, with minimum concentrations observed during day time between 3 and 5 pm and maximum concentrations during late night and early morning hours (6–9 am). However, urban sites (IITD and IITMDD) exhibited more distinct diurnal patterns as compared to urban downwind site (MRIIRS), which could be attributed to the proximity of the urban site to primary emission sources and mixing and aging of air masses during transport to the urban background site located in the downwind direction, making the variation less pronounced. Similar differences in diurnal variation between urban and urban background sites were observed by Crippa et al. (2013a) in the Paris metropolitan area. Organics and BC showed a sharp increase in concentration from ~5 pm till ~11 pm and a small increase during early morning hours (6–9 am). This could be attributed to a combination of reduced atmospheric mixing with a decrease in the atmospheric boundary layer and an increase in solid fuel combustion activities such as the burning of wood, coal, and roadside trash for heating purposes, and traffic emissions

during rush hours. Owing to the decrease in PBL and increased formation at lower temperatures, semi-volatile species such as nitrate, ammonium, and chloride concentration increased from late evening till morning at all sites with a sharp peak between 6 and 8 am.

3.2. OA source apportionment results

In this section, we describe the selection criteria for choosing the optimum PMF solution for each site, OA factors identified in terms of their mass spectra, diurnal and temporal variation, and correlation with external tracers. For the first time in the present study, using the HR-ToF-AMS data for IITD and MRIIRS sites, we have used the combined HR (ions from m/z 12 to 120) and UMR (m/z 121 to 350 for IITD and m/z 120 to 300 for MRIIRS) spectra for the PMF analysis, which resulted in PMF factors having signals of higher m/z's (>120). This enabled us to identify polycyclic aromatic hydrocarbons (PAH) fragments at high m/z's (178 and 202) and separate two semi-volatile oxygenated OA (SV-OOA), and two solid-fuel combustion (SFC) factors based on the differences in their mass spectra in the high m/z region along with other criteria (discussed in detail in Section 3.2.2).

3.2.1. Selection of optimum PMF solution

The optimum solution was chosen based on the significant signal intensity of specific marker ions of sources in the factor mass spectra, correlation of factor time series with external measurements, elemental ratios of the factor mass spectra, and physical interpretability of the factors. Also, Q/Q_{exp} and residuals were investigated.

The procedure followed for selecting the optimum PMF solutions for IITD and MRRIRS are described in detail in the Supplementary information (S-1 and S-2), respectively, and are briefly discussed here. For the IITMDD site, the optimum solution is directly taken from our companion paper (Tobler et al., 2020), where OA mass spectra was best represented by three factors, namely hydrocarbon-like OA (HOA), solid-fuel combustion (SFC) OA, and oxygenated OA (OOA). The HOA profile in the unconstrained 3-factor solution contained signals of both SFC and HOA
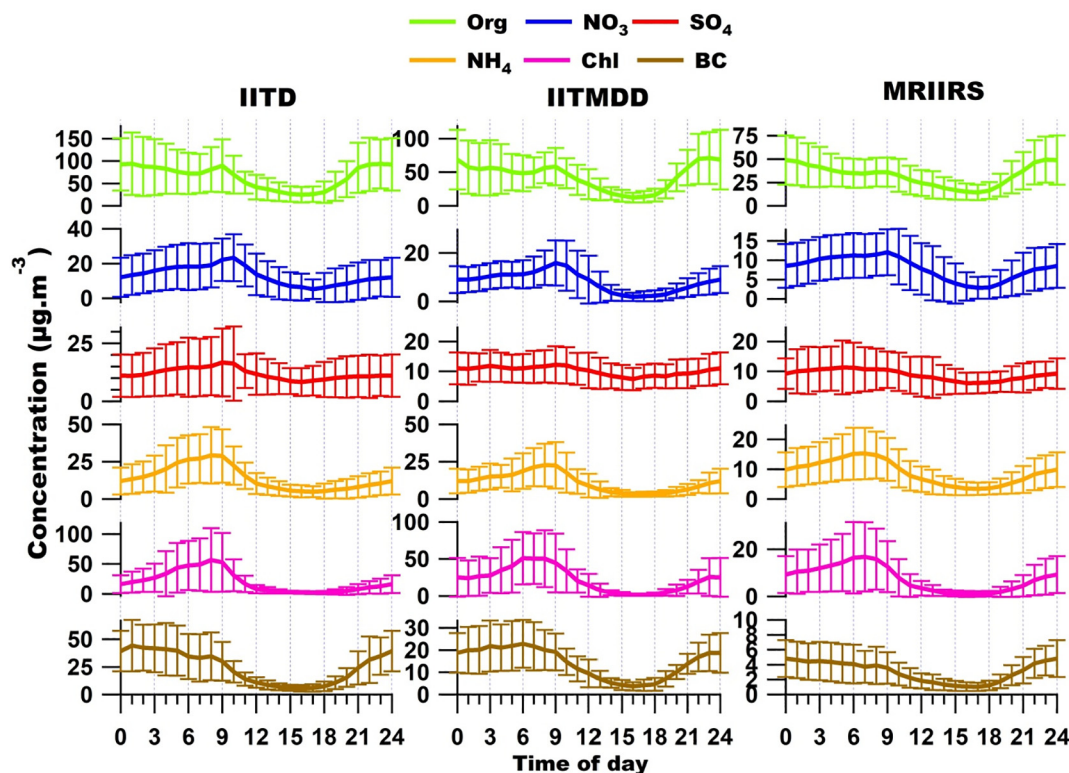

Fig. 3. Diurnal variation of mass concentration of PM species measured at IITD, IITMDD and MRIIRS site.

factor. So, a clean external HOA profile found in Paris by Crippa et al. (2013b) was used to constrain one factor (HOA) with a random *a*-value varying from 0 to 0.5. A detailed description of the HOA optimization for the IITMDD site has been described in Tobler et al. (2020). The higher 4-factor solution resulted in an additional primary factor with mass spectral characteristics of both HOA and SFC-OA, and the 5-factor solution resulted in an additional OOA factor split from the OOA factor in the 3-factor solution (Tobler et al., 2020). For the IITD site, in the 5-factor solution, a lot of primary species contributed to a likely semi-volatile oxygenated OA (SV-OOA) factor, whereas in the 7-factor solution, a split in the SFC factor was observed without a significant increase in explained variability. Further, the difference in the Q$_{residual}$ value when moving from one factor (lower) to another (higher) factor solution was inspected (Fig. S3), which indicates the increase in the explained variability with the added factor. The largest differences were

observed when moving from 5-factor to 6-factor solution. Thus, based on the above observations and the environmental feasibility of the factors, a 6-factor solution was chosen as the most optimum solution. For the MRIIRS site, a significant percent decrease in Q/Q$_{exp}$ when moving to a higher number of factors solution (>15%) was observed up to a 3-factor solution but decreased to <5% when going up from 3 to 4 (Fig. S4). This suggested significant variability in the data was explained until the 3-factor solution, which was chosen as the minimum number of factors. In the 5-factor solution, a high signal of m/z 60 (0.0075) (tracer of biomass burning) was found in a likely HOA factor, whereas in the 7-factor solution, an additional factor was split from a SFC factor in the 6-factor solution as shown in Fig. S7. Therefore, a 6-factor solution was chosen as the optimum solution from the unconstrained PMF run. But, the HOA factor in the unconstrained solution was not clearly resolved, and had high CO_2^+ (m/z 44) and $C_2H_4O_2^+$ (m/z 60) intensity.
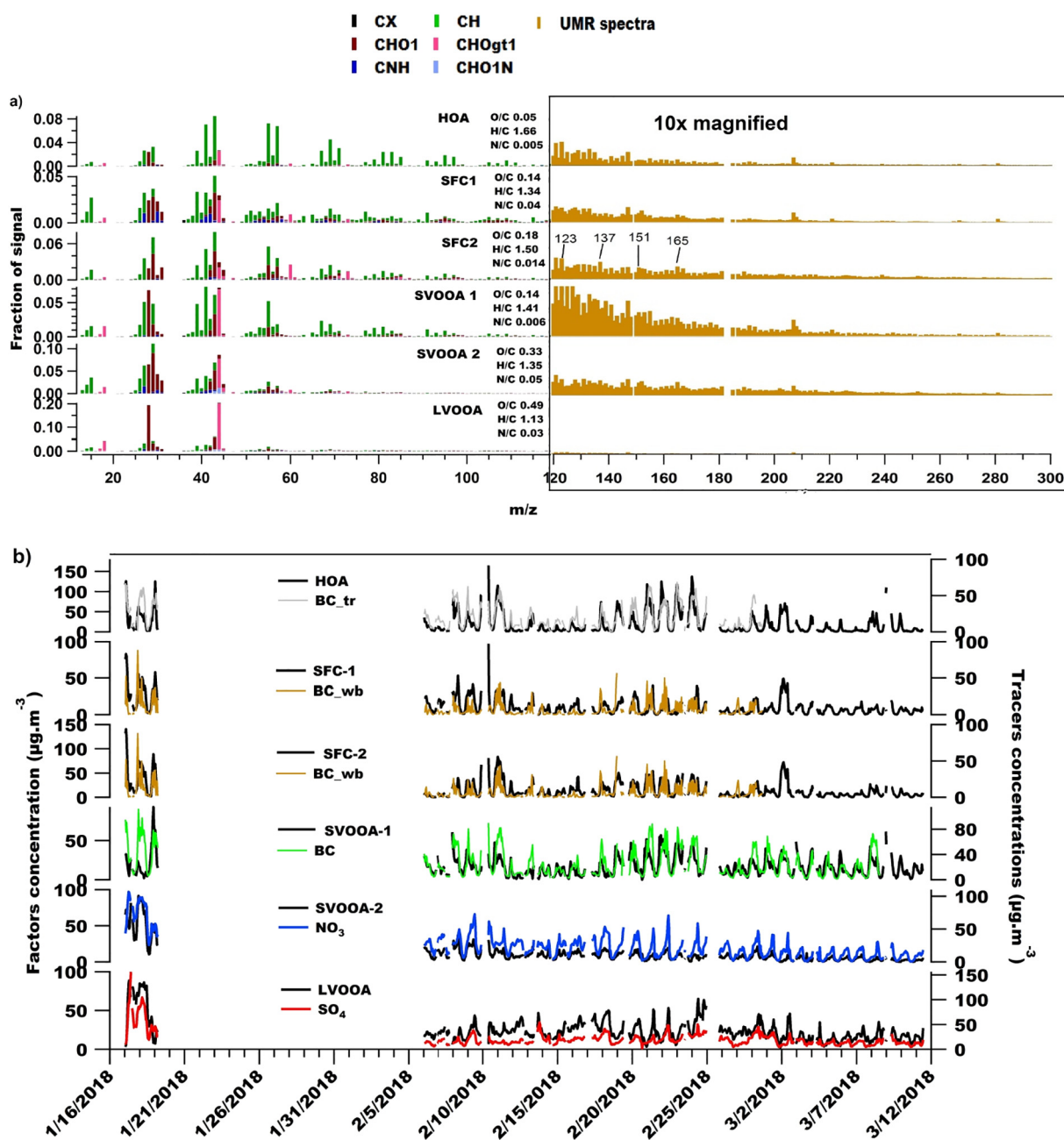

Fig. 4. a) Mass spectra of OA factors identified at IITD site (UMR spectra is shown separately on the right with brown color to clearly show the lower intensity signals at m/z 120 to 350); b) temporal variation of hourly averaged mass concentration of OA sources in µg.m^{-3} (left axis) identified at IITD site. Right axis represents the concentration of external tracers. (For interpretation of the references to color in this figure legend, the reader is referred to the web version of this article.)

Thus, a constrained PMF run was performed with six factors, and values of CO_2^+ and $C_2H_4O_2^+$ were constrained to "0" in only one factor (HOA), and a-value varied from 0 to 1 with a-delta as 0.1, producing 11 PMF solutions each with different a-value. Finally, the solution with a-value = 0.6 was chosen as the best solution based on tracers identified in the mass spectra, O/C of HOA, and temporal correlation of HOA with BC.

3.2.2. PMF results

For IITD and MRIIRS, OA mass spectra from HR-ToF-AMS (combined HR and UMR) was factorized into 6-factors consisting of HOA, two SFC factors (SFC-1 & SFC-2), two SVOOA factors (SVOOA-1 & SVOOA-2), and one low-volatile oxygenated OA (LVOOA) factor, whereas at IITMDD, UMR OA spectra from ToF-ACSM was factorized into three factors including HOA, SFC and oxygenated OA (OOA). The difference in the number of OA factors was probably due to the higher mass resolving power of HR-ToF-AMS ($\Delta M/M \sim 2100$ at m/z 200) (DeCarlo et al., 2006), as compared to ToF-ACSM ($\Delta M/M = 600$) (Fröhlich et al., 2013). Figs. 4-6 show the mass spectra and time series of the OA factors identified for IITD, IITMDD, and MRIIRS, respectively.

HOA mass spectra was characterized by signals of aliphatic hydrocarbons at m/z 41 (C_3H_5), 43 (C_3H_7), 55 (C_4H_7) and 57 (C_4H_9), 69 (C_5H_9) and 71 (C_5H_{11}), which are typically associated with traffic exhaust emissions (Canagaratna et al., 2007; Ng et al., 2011). A low O/C of 0.05 was observed for both IITD and MRIIRS sites, which is close to the value for gasoline and diesel exhaust, and consistent with other studies (Mohr et al., 2009; Zhang et al., 2011). This was not possible in the earlier studies using conventional PMF 2 resulting in either higher O/C value in the HOA factor or a mixed factor containing signals of both HOA and cooking OA, or HOA and biomass burning OA (Chakraborty et al., 2015; Kumar et al., 2016; Thamban et al., 2017).

At the IITD site, Bhandari et al. (2020) resolved a mixed HOA and BBOA factor by applying PMF2 on Q-ACSM data during 2017.

Fig. 7 shows the diurnal variation of the OA factors identified at the three sites averaged over the campaign period for each site. HOA factor exhibited a strong diurnal cycle at all sites with a small morning rush hour peak between 9 and 10 am and a sharp peak in the evening between 6 and 11 pm. Unlike MRIIRS, high overnight concentrations were observed at IITD and IITMDD sites indicating high night-time vehicular emissions at the two urban sites. This could be attributed to the heavy-duty vehicles which are only allowed in the city premises from 11:00 to 17:00 and 21:30 to 07:30. HOA and BC_{tr} followed similar temporal trends for IITD and IITMDD sites (Figs. 4b & 5b) with R^2 value of 0.49 for IITD (Fig. S8) but a relatively lower correlation value ($R^2 = 0.27$) was found for IITMDD (Fig. S9), which was because BC_{tr} did not follow certain high concentration peaks in HOA concentration (Fig. 5b). While, for MRIIRS, a correlation value of 0.56 was found between HOA and BC (Fig. S10).

SFC at IITMDD contained significant signals at m/z 60 and m/z 73, which are associated with biomass burning (Alfarra et al., 2007; Simoneit et al., 1999), along with signals of unsaturated hydrocarbons at m/z 77, 91, and 115, and PAH at m/z 178 and 202, which typically come from combustion processes (Fig. 5a). From HR-AMS data at IITD and MRIIRS, we were able to resolve two SFC factors (SFC-1 and SFC-2). The two SFC factors were characterized by signals of anhydrous sugars at m/z 60 ($C_2H_4O_2$) and m/z 73 ($C_3H_5O_2$), and other oxidized fragments at m/z 29 (CHO), m/z 43 (C_2H_3O), and m/z 44 (CO_2). O/C of 0.14 and 0.25 were observed for SFC-1, whereas 0.18 and 0.19 in the case of SFC-2, for IITD and MRIIRS, respectively. The main difference between SFC-1 and SFC-2 mass spectra was the presence of ions with different delta (Δ) patterns for $m/z > 44$, where $\Delta = M_{m/z}-14n + 1$
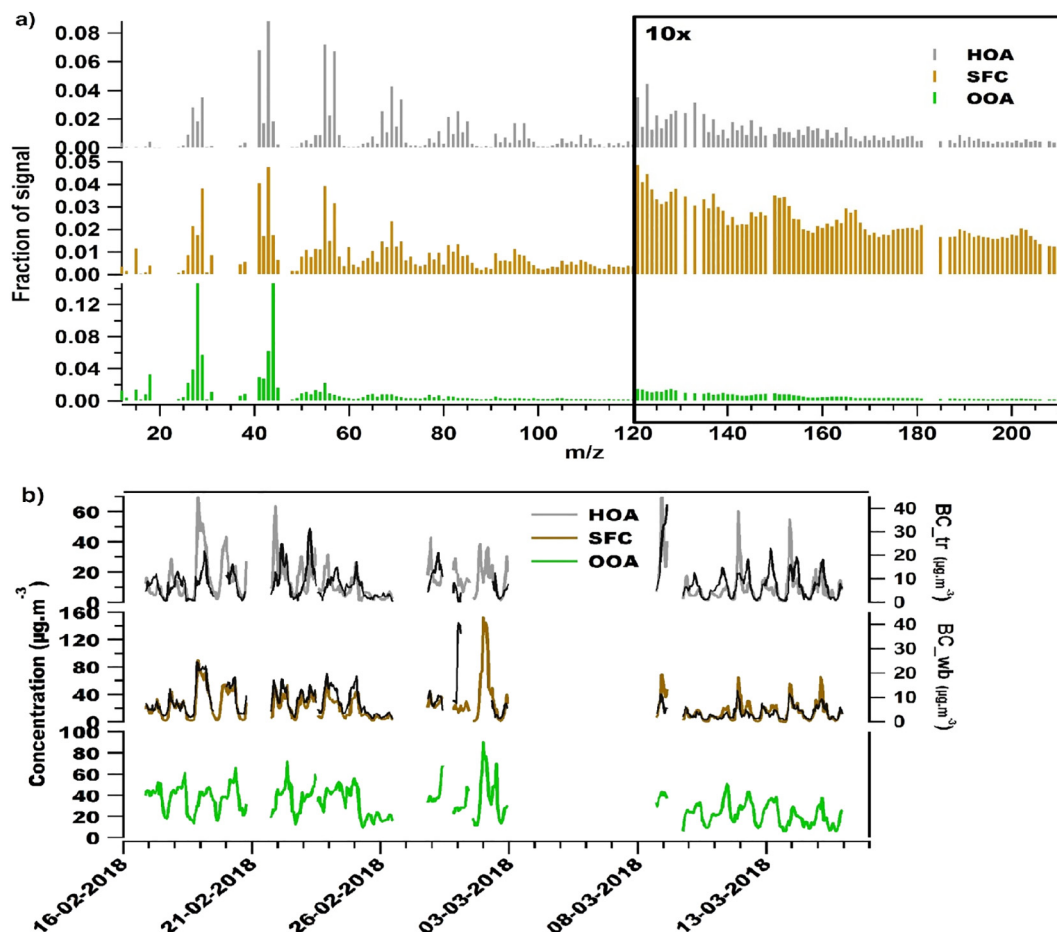

Fig. 5. (a) Mass spectra and (b) time series of OA factors at IITMDD site. Left axis represents concentration of OA factors whereas right axis represents concentration of external tracers.
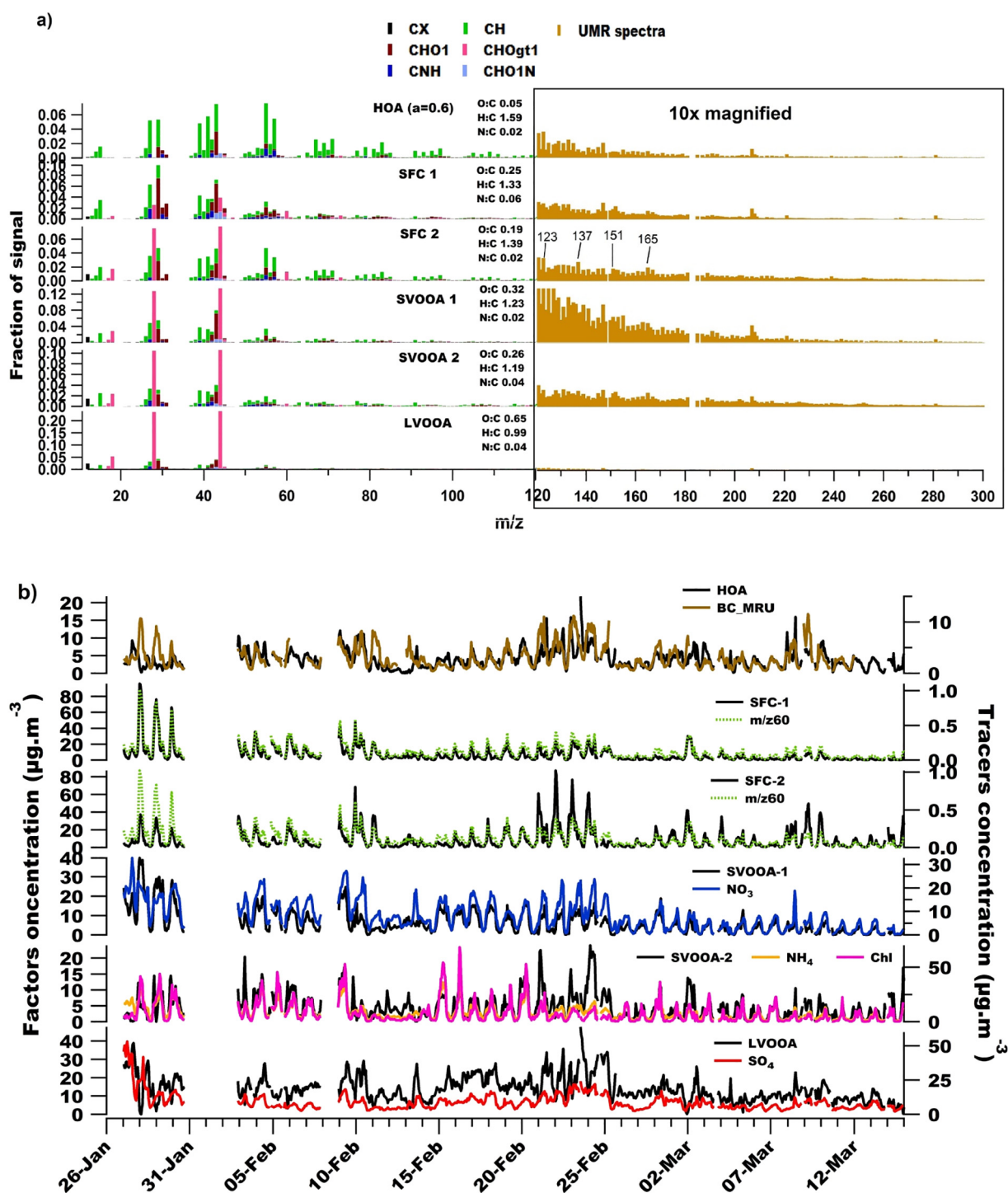
Fig. 6. Mass spectra (a.) and temporal variation (b.) of OA factors identified at MRIIRS site (UMR spectra in a) is shown separately on the right with brown color to clearly show the lower intensity signals at m/z 120 to 350. Left axis represents the concentration of OA factors whereas right axis represents the concentration of external tracers. (For interpretation of the references to color in this figure legend, the reader is referred to the web version of this article.)

($M_{m/z}$ is the mass of the ion and n is the number of carbon atoms present). SFC-1 included ions at m/z 63 (C_5H_3), 77 (C_6H_5), 91 (C_7H_7), 105 (C_8H_9), and 119 (C_9H_{11}), all with Δ value of −6. Along with prominent peaks from aromatic hydrocarbons at m/z 77 (C_6H_5), m/z 91 (C_7H_7) and m/z 115 (C_9H_7), which are associated with coal combustion (Dall'Osto et al., 2013; Elser et al., 2016), SFC-1 also contains small contributions at m/z 178 and m/z 202, which are associated with polycyclic aromatic hydrocarbons (anthracene and pyrene), and are typically emitted from incomplete combustion processes. This indicates SFC-1 to be influenced more from a mixture of coal-burning for residential heating and

burning of roadside trash including leaves, compostable waste, etc., which usually involves incomplete combustion. In addition, SFC-1 exhibited high N/C value of 0.04 and 0.06 for IITD and MRIIRS, respectively, with significant amines signal at m/z 27 (CHN), m/z 30 (CH_4N), m/z41 (C_2H_3N), m/z 42 (C_2H_4N), m/z 52 (C_3H_2N), m/z 54 (C_3H_4N), m/z 56 (C_3H_6N) and m/z 58 (C_3H_8N).

On the other hand, SFC-2 included ions at m/z 53 (C_4H_5), 67 (C_5H_7), 81 (C_6H_9), 95 (C_7H_{11}), 109 (C_8H_{13}), all with Δ value of −2. In continuation of the HR ions with Δ = −2, peaks at m/z 123, 137, 151, 165 were also observed, with the subsequent addition of the CH_2 group. In
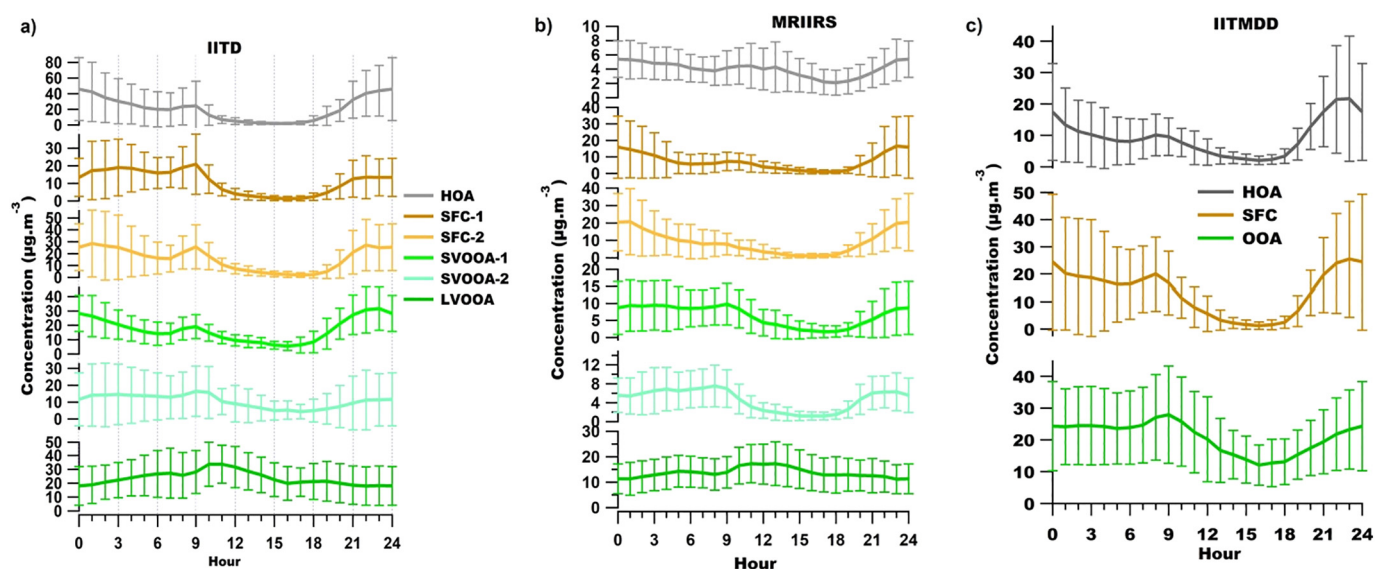
Fig. 7. Average diurnal variation of mass concentration of OA factors at a) IITD (17th January-19th January & 5th February-11th March, 2018); b) MRIIRS (27th January - 15th March, 2018) and c) IITMDD (17th February – 15th March, 2018).

addition, SFC-2 mass spectra also included prominent signals from aliphatic hydrocarbons at m/z 41, 43, 55, and 57, which are also found in mass spectra of conventional biomass burning emissions such as wood and paper (Mohr et al., 2009). Signals of aromatic fragments at m/z 77 (C_6H_5), m/z 91 (C_7H_7), and m/z 115 (C_9H_7) were also observed but with lower intensities as compared to SFC-1. Thus, we argue that SFC-2 is probably more affected by conventional biomass burning emissions.

SFC at all three sites showed similar diurnal behavior with a small peak in the morning between 7 and 9 am whereas a large peak in the evening between 6 and 11 pm, which is consistent with residential heating and burning activities. A very low daytime concentration was observed for all sites which could be attributed to less solid-fuel burning emissions during the day, and increase in PBL leading to increased mixing. Time series of SFC at IITMDD correlated well with BC_{wb} ($R^2 = 0.79$) (Fig. S9), while for IITD, lower correlation values were obtained for SFC-1 ($R^2 = 0.20$) and SFC-2 ($R^2 = 0.34$) with BC_{wb} (Fig. S8). However, similar temporal trends for SFC and BC_{wb} can be seen for both sites in Figs. 4b and 5b. For MRIIRS, SFC-1 and SFC-2 correlated strongly with AMS measured m/z 60 with R^2 values of 0.71 and 0.85, respectively (Fig. S10). Similar contribution of SFC were observed at IITMDD (~30.5%), IITD (SFC-1:11.4% and SFC-2: 16.2%) and MRIIRS (SFC-1:16.1% and SFC-2: 19.7%) (Fig. 8).

SVOOA-1 and SVOOA-2 were characterized by higher signals of oxidized fragments at m/z 44 (CO_2) and m/z 43 (C_2H_3O), as compared to primary OA factors (HOA and SFC). SVOOA-1 mass spectra was dominated by ions at m/z 53 (C_4H_5), 67 (C_5H_7), 81 (C_6H_9), 95 (C_7H_{11}), 109 (C_8H_{13}), all with Δ value of −2, along with aromatic fragments at m/z 63 (C_5H_3), 77 (C_6H_5), 91 (C_7H_7), 105 (C_8H_9), all with Δ value of −6. The presence of aromatic compounds suggests that it could be because of the oxidation of primary emissions rich in aromatic content such as vehicular. Whereas, SVOOA-2 included nitrogen-containing fragments (CHN and CHNO) at m/z 27, 30, 40, 41, and 42 with high N/C of 0.05 and 0.04 for IITD and MRIIRS, respectively, along with traces of biomass burning fragments at m/z 60 and 73. This suggests it could be formed from the oxidation of biomass burning emissions. SVOOA-2 also included aromatic fragments at m/z 77, 91, and 115, but with lower intensity. This indicates the two factors were formed by the oxidation of different types of precursor compounds. As compared to the highly oxidized LVOOA (0.49 and 0.65) factor, much lower O/C values of 0.14 and 0.32 for SVOOA-1, while 0.33 and 0.26 were observed for SVOOA-2, for IITD and IITMD sites, respectively, indicating their freshly oxidized nature. Both SVOOA-1 and SVOOA-2 exhibited strong diurnal behavior with a small peak in the morning at around 9 am, which could be attributed to formation due to photochemical oxidation, and a large peak in the evening between 6 pm and 11 pm, which could be attributed to gas to particle partitioning with decreasing temperatures and increasing relative humidity. Low concentration during day time could be because of increased atmospheric mixing due to an increase in PBL. As compared to other species, the SVOOA-1 time series correlated only with AMS nitrate ($R^2 = 0.33$) in the case of MRIIRS, and with BC ($R^2 = 0.36$) in the case of IITD. Whereas, SVOOA-2 correlated strongly with AMS nitrate
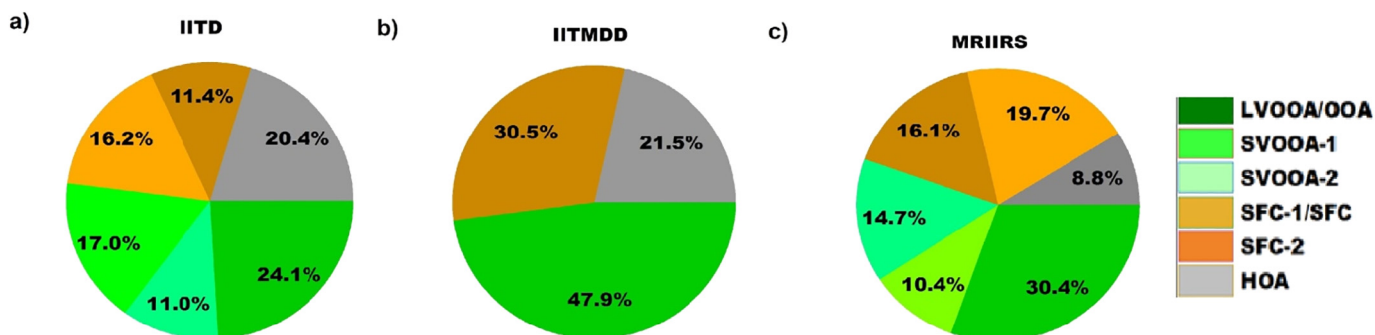

Fig. 8. Average percent contribution of OA factors to total OA mass at a) IITD; b) IITMDD; and c) MRIIRS site.

($R^2 = 0.76$) in the case of IITD, and less with AMS ammonium ($R^2 = 0.35$) and chloride ($R^2 = 0.33$) in the case of MRIIRS. Good temporal correlations of SVOOA-1 and SVOOA-2 with semi-volatile nitrate, ammonium, and chloride further support their semi-volatile nature. SVOOA-1 comprised around 17% and 14.7% of total organic mass whereas SVOOA-2 comprised 11% and 10.4% for IITD and MRIIRS sites, respectively (Fig. 8).

LVOOA was characterized by very high signals at m/z 44 (CO_2^+), relatively less signal at m/z 43 ($C_2H_3O^+$), and negligible signals at $m/z > 44$ indicating the aged nature of this factor (Ng et al., 2010). High O/C of 0.49 and 0.65 were observed for IITD and MRIIRS, respectively. LVOOA at the IITMDD site was also dominated by m/z 44 signals with small aliphatic hydrocarbon signals at m/z > 44, which is also evident from slightly strong diurnal variation as compared to IITD and MRIIRS. The diurnal patterns for IITD and MRIIRS showed relatively stagnant and elevated concentrations throughout the day. A peak in the concentration was observed between 9 and 11 am at IITD, whereas for a longer duration (9 am - 3 pm) at MRIIRS, which could be attributed to production of secondary organics from photochemical oxidation, after which a decreasing trend was observed, which could be attributed to increasing planetary boundary layer height (PBLH). Time series of LVOOA at IITD correlated strongly with AMS measured both sulfate (SO_4^{2-}) ($R^2 = 0.82$) and nitrate (NO_3^-) (0.78) (Fig. S8), whereas relatively less for MRIIRS ($R^2 = 0.47$ with SO_4^{2-} and 0.40 with NO_3^-, Fig. S10) further supports the aged nature of this factor. Overall, a similar fractional contribution of SOA (LVOOA + SVOOA-1 + SVOOA-2) to the total OA mass was observed at the three sites with average campaign percent contribution for IITD, IITMDD, and MRIIRS as 52.1%, 47.9%, and 55.5%, respectively (Fig. 8).

3.3. Comparison of OA sources at three sites

In this section, we compare the mass spectra of OA factors identified at the three sites. Further, an overlapping period of sampling from three sites (17 February-11 March, 2018) was selected to compare the temporal and diurnal variation, and percent contribution of the factors to the total OA mass. Overall, OA mass spectra at IITD and MRIIRS was resolved into three oxidized factors including one low-volatile and two semi-volatile factors, constituting total OOA, whereas only one oxidized OA factor was obtained at the IITMDD site. Furthermore, two SFC factors with different chemical fingerprints were resolved at IITD and MRIIRS as opposed to one SFC factor at IITMDD. This was mainly due to the higher mass resolution of the L-ToF-AMS and HR-ToF-AMS, compared to the ToF-ACSM, as discussed in Section 3.2.2. For IITD and MRIIRS, three oxidized factors (LVOOA, SVOOA-1, and SVOOA-2) were summed to calculate total OOA, while two solid-fuel combustion factors (SFC-1 and SFC-2) were summed to calculate total SFC, for comparison with respective IITMDD factors (OOA, SFC, and HOA).

A cooking OA (COA) factor was not identified at any of the sites. A COA factor mass spectra is similar to HOA but has some key differences such as a higher ratio of m/z 55 to m/z 57, high contribution of oxygen-containing ions at m/z 43, 55, and 57, higher O/C value (~0.2) than HOA factor (~0.05) (He et al., 2010; Mohr et al., 2009). We found very low m/z (55/57) values for HOA at IITD and IITMDD (1.06–1.07) but slightly higher in the case of MRIIRS (1.3). Further, the oxidized CHO group ions were also present in the HOA mass spectra at m/z 43, 55, and 57 at the MRIIRS site as opposed to the IITD site suggesting that it could be mixed with COA related emissions. The diurnal variation of HOA at IITD and IITMDD did not show any peak during the lunch hours (Fig. 9d) which is distinctly observed in the COA factor (He et al., 2010; Mohr et al., 2012). However, a distinct peak during lunchtime (~1 pm) was observed in the HOA diurnal pattern at the MRIIRS site during the afternoon (Fig. 9d) which could likely be because of cooking-related emissions from the hostel mess and canteen in the MRIIRS campus. This suggests that the HOA factor at MRIIRS was probably mixed with COA, however, the low O/C value (0.05), the

dominance of hydrocarbon series in the mass spectra and good correlation with BC supports our nomenclature of this factor (Ng et al., 2010).

Fig. 9 shows the comparison of the diurnal variation of (a) OOA, (b) SVOOA, (c) SFC, and (d) HOA factors between the three sites. Temporal correlation between OA factors at the three sites was investigated for the whole common period (overall) and further by dividing into rush hours (7 am–10 am and 6 pm–11 pm), mid-day hours (12 pm–6 pm), and over-night hours (12 am–6 am) to investigate the effect of local emissions on the correlation. Table S1 shows the correlation (Pearson's R^2) between OA factors identified at the three sites during rush-hour, mid-day, overnight, and overall.

A large difference in HOA concentration was observed between IITD, IITMDD, and MRIIRS with average values of $26.7 \pm 29.2 \, \mu g.m^{-3}$, $15.6 \pm 13.3 \, \mu g.m^{-3}$, and $5.0 \pm 2.7 \, \mu g.m^{-3}$, respectively. Wang et al. (2020) based on PTR-ToF-MS data, also found that the nocturnal mixing ratio of primary VOCs at the IITD site was twice that of the MRIIRS site. Overall, the HOA time series correlated reasonably well between IITD and IITMDD ($R^2 = \sim 0.3$–0.4) during overall, rush hours and over-night hours, but decreased significantly during the mid-day hours ($R^2 = 0.13$). Correlation between IITMDD and MRIIRS was not good during overall, rush-hour and over-night ($R^2 = 0.07$–0.10) but increased for mid-day hours ($R^2 = 0.37$) when concentration levels were low. Similarly, between IITD and MRIIRS, correlation varied significantly between different times of day ($R^2 = 0.15$ to 0.32). Relatively higher HOA concentrations were observed at night as compared to the day, which could be related to nighttime traffic emissions from heavy-duty vehicles (only allowed in the city during). Significant differences in the absolute concentration and temporal correlation between the three sites during different times of day indicate HOA to be largely driven locally with the highest fractional OA mass contribution at IITD (25%) followed by IITMDD (21%) and MRIIRS (10%). The CWT plots for HOA for all three sites indicated the probable source to be of local origin (Figs. S13–15).

SFC-2 at MRIIRS is located higher and more to the left on f_{44} (ratio of signal at m/z 44 to the total organic signal of factor mass spectra) vs f_{43} (defined as that of f_{44}) than SFC-2 at IITD (Fig. S12) indicating it to be more oxidized (Ng et al., 2010). SFC-1 mass spectra at MRIIRS had higher signals from oxygenated fragments (CHO and CHOgt1) whereas less signals from aliphatic hydrocarbons, with higher O/C of 0.25 than IITD (0.14), indicating it to be more oxidized at the downwind location. Furthermore, in addition to CHN fragments observed at both sites, CHNO fragments (m/z 43, 44) were also present in the case of MRIIRS, which could be due to oxidation of nitrogen-containing fragments. At MRIIRS, the signal intensity of aromatic fragments at m/z 77, 91, and 115 was similar in SFC-1 and SFC-2, unlike IITD, which could be attributed to more mixing of the air masses at the downwind location. Both SFC-1 and SFC-2 had higher N/C of 0.06 and 0.02 at MRIIRS, as compared to 0.04 and 0.014 at IITD, respectively. SFC-1 exhibited increasing nighttime concentration at IITD whereas a decreasing trend at MRIIRS was observed, indicating higher SFC-1 emissions at IITD. Unlike HOA, similar SFC concentration levels were observed at the three sites, with highest at IITD (SFC-1 + SFC-2) ($27.9 \pm 23.3 \, \mu g.m^{-3}$) followed by IITMDD ($25.1 \pm 23.8 \, \mu g.m^{-3}$) and MRIIRS (SFC-1 + SFC-2) ($19.2 \pm 20.7 \, \mu g.m^{-3}$). SFC correlated strongly between IITD and IITMDD ($R^2 = 0.70$) as compared to IITD and MRIIRS ($R^2 = 0.42$) and IITMDD and MRIIRS ($R^2 = 0.27$). Correlation between IITD and IITMDD increased during overnight hours ($R^2 = 0.81$) indicating similar SFC emissions at the two sites, whereas decreased between IITMDD and MRIIRS, and IITD and MRIIRS. This is also visible from the similar diurnal trend of SFC at IITMDD and the sum of SFC-1 and SFC-2 at IITD, whereas a decreasing trend was observed at MRIIRS (Fig. 9c), indicating it to be less affected by SFC emissions at night. The CWT plots for SFC-1 shows it to be affected both from the transported air masses from the north-west direction and close to the proximity to the sampling site, whereas the probable source of high concentrations for SFC-2 appears to local (Figs. S13 & S15). The CWT plot for SFC at IITMDD shows that it was affected both from transported air masses from the north-west direction
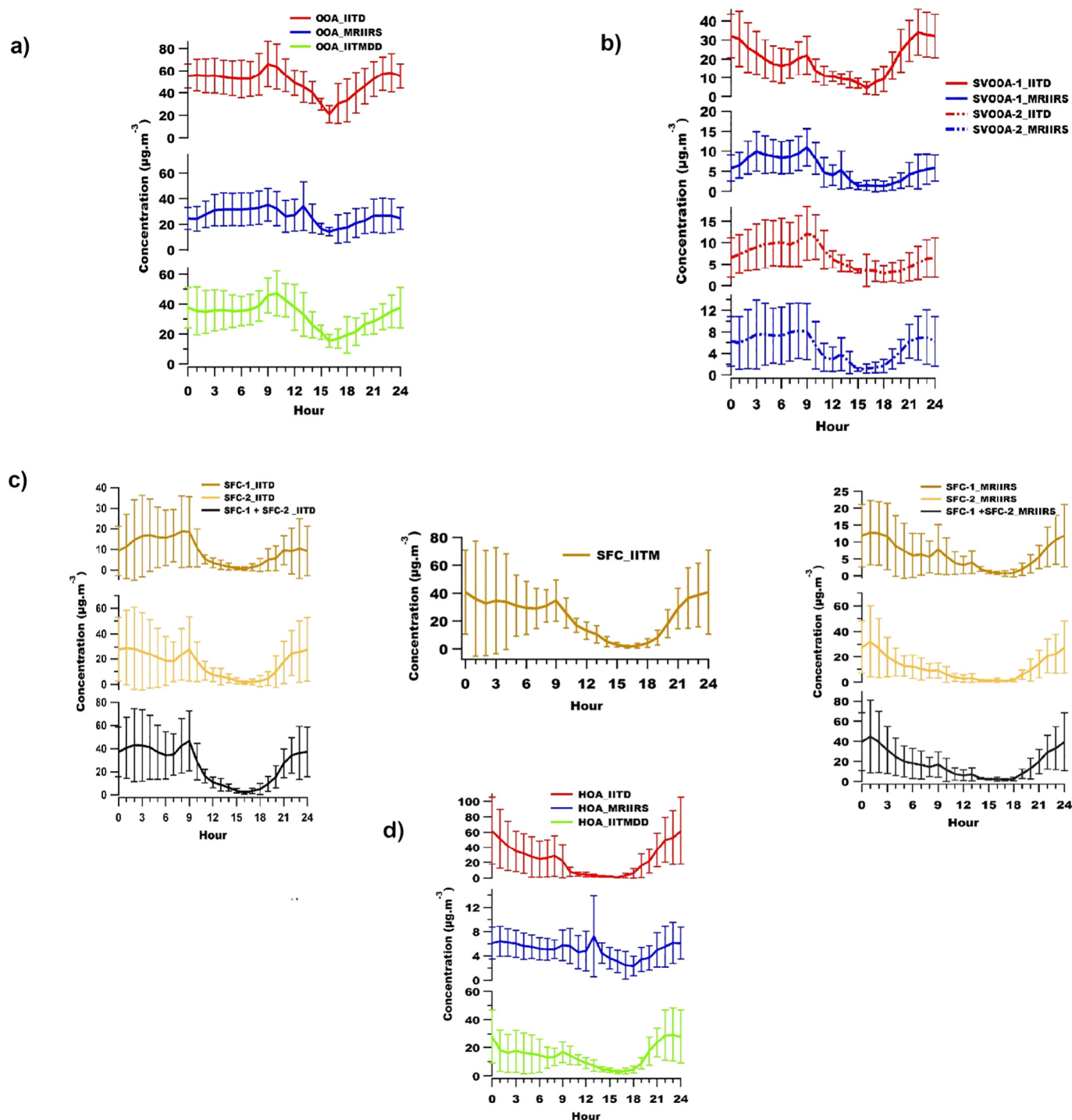
Fig. 9. Comparison of average diurnal variation of mass concentration of OA factors a) LVOAA; b) SVOOA; c) SFC; and d) HOA at IITD, IITM, and MRIIRS for the common sampling period between the three sites (17th February – 11th March, 2018).

and proximity to the sampling site (Fig. S14). Overall, different mass spectral characteristics of SFC-1 and SFC-2 and diurnal behavior indicates that the two factors were influenced by different types of solid-fuel burning emissions. SFC-1 included aromatic and PAH fragments and ions with $\Delta = -6$, and was probably more affected by incomplete combustion emissions such as burning coal and roadside trash, whereas SFC-2 included ions with $\Delta = -2$ and aliphatic hydrocarbons, and was probably more affected from wood-burning emissions. While SFC at IITMDD was probably influenced by a combination of SFC-1 and SFC-2 emissions sources.

High spectral similarity was observed between OOA factors at IITD and MRIIRS ($R^2 = 0.60$–0.98) (Fig. S11). Both SVOOA-1 and SVOOA-2 had higher O/C for MRIIRS than IITD, and were located higher and more to the left on f_{44} vs f_{43} plot, indicating it to be more oxidized at the downwind location (Fig. S12). The mass spectra of SVOOA-1 was dominated by ions with $\Delta = -2$ and -6, which included fragments of aromatic compounds, whereas SVOOA-2 was rich in nitrogen-containing compounds with higher N/C values. However, unlike IITD, SVOOA-1 at MRIIRS had similar or higher signal intensities of aromatic fragments at *m/z* 77, 91, and 115 than SVOOA-2. Furthermore, the two

factors had large differences in their O/C (0.14 and 0.33 for SVOOA-1 and SVOOA-2, respectively) and N/C (0.006 and 0.02) values at IITD, as compared to MRIIRS, where similar O/C (0.32 and 0.26) and N/C (0.02 and 0.04) were observed. This could be attributed to the mixing of the freshly oxidized factors at the downwind site. At both IITD and MRIIRS sites, SVOOA-1 and SVOOA-2 showed a small peak in concentration at 9 am (Fig. 9b), indicating formation due to photochemical oxidation probably from primary gaseous and particulate emissions related to traffic and solid fuel burning. SVOOA-2 showed a similar diurnal pattern at the two sites with concentration increasing from late evening and maintaining stable concentration during the night. Overall, significant differences in the mass spectra and diurnal patterns suggest that SVOOA-1 and SVOOA-2 were formed from different precursor compounds, with SVOOA-1 affected more from the oxidation of primary emissions rich in aromatic content, whereas SVOOA-2 from the oxidation of solid-fuel burning emissions. The CWT plot for SVOOA-1 shows the probable source of high concentration in the north-west and local for both IITD and MRIIRS (Figs. S13 & S15). While for SVOOA-2, the probable source at IITD is more local and from the south-east direction, whereas, at MRIIRS, it appears to be originated from the north-west and local sources.

f_{44} vs f_{43} plot showed that LVOOA at MRIIRS was the most oxidized with O/C of 0.65 followed by LVOOA at IITD with O/C of 0.49 (Fig. S12). Unlike the LVOOA factor obtained at IITD and MRIIRS, OOA at IITMDD showed some aliphatic signals at high m/z's, indicating that it contains signals of both freshly and highly oxidized OA obtained at IITD and MRIIRS. This is also evident from the similar diurnal trend of OOA at IITMDD and total OOA at IITD (LVOOA+SVOOA-1 + SVOOA-2) (Fig. 9a), which showed a small peak at 9 am, suggesting its formation from photochemical oxidation. However, LVOOA at MRIIRS showed

a relatively more stable diurnal pattern and a second peak at 1 pm, which could be attributed to more photochemical oxidation at the downwind site, or the influence of transported air mass from upwind urban sites (IITD and IITMDD). The CWT plot for LVOOA at IITD showed the probable source of high concentrations located in the south-east and in close proximity to the sampling site, whereas at MRIIRS, it appears to be originated from close proximity and north-west direction (Figs. S13-S15). While the OOA factor at IITMDD appears to be affected by both north-west direction and close proximity to the sampling site.

Significant differences were observed in the average OOA concentration levels (calculated for the common sampling period) between the three sites with highest at IITD (50.9 ± 18.1 μg.m^{-3}) followed by IITMDD (32.96 ± 13.45 μg.m^{-3}) and MRIIRS (27.04 ± 12.68 μg.m^{-3}). Overall, OOA correlated reasonably well between the three sites with the highest value for IITD and MRIIRS ($R^2 = 0.54$) followed by IITD vs IITMDD ($R^2 = 0.47$) and IITMDD vs MRIIRS ($R^2 = 0.36$). No significant change in correlation was observed with different time of day other than a decrease between IITD and IITMDD during overnight hours, indicating it to be less affected by primary emissions. However, in the Paris metropolitan area, observed similar concentrations levels and much higher correlation ($R^2 = 0.7–0.9$; slope = ~0.9–1.1) between OOA at the urban core and urban background sites, thus indicating the dominance of regional sources on Paris air quality Crippa et al. (2013a). Another study conducted in summer 2009 using AMS measurements at three sites over Paris megacity found similar concentrations of secondary OA (Freutel et al., 2013). These differences in the absolute concentrations of OOA at the three sites in Delhi-NCR suggest the influence of local emissions on air quality.

OOA was the dominant fraction of total OA mass at all sites constituting on average 48%, 45%, and 53% at IITD, IITMDD, and MRIIRS sites,
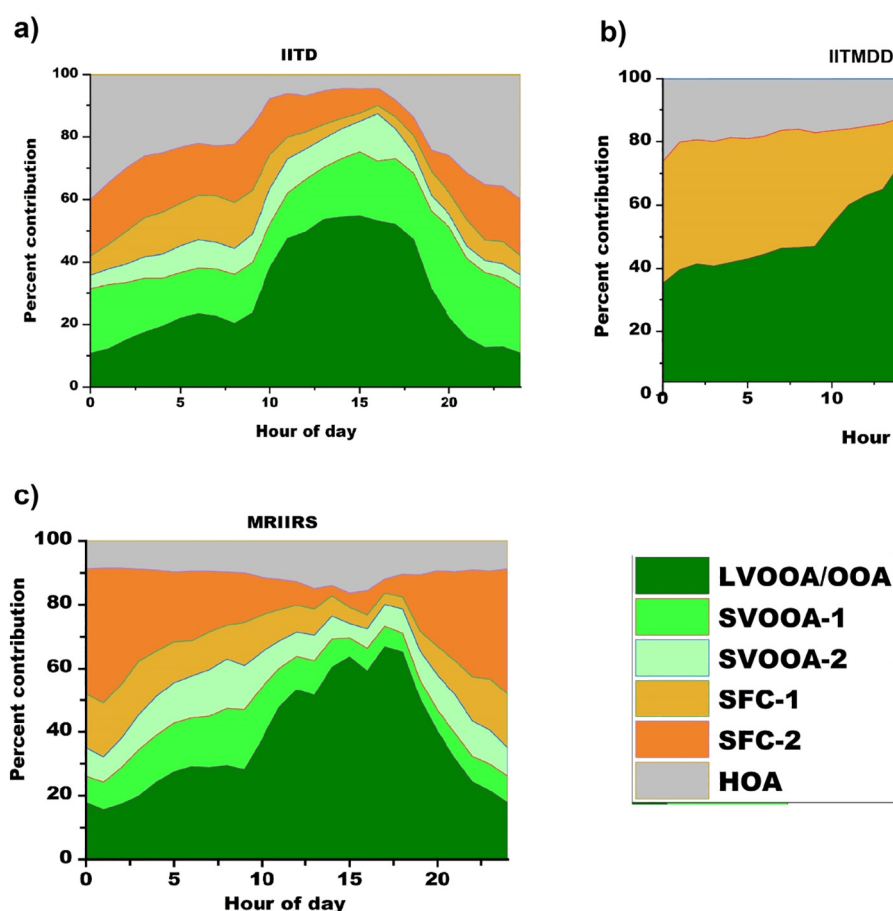

Fig. 10. Diurnal variation of percent contribution of OA factors to the total OA mass at a) IITD, b) IITMDD, c) MRIIRS.

respectively (calculated for the common sampling period). Fig. 10 shows the diurnal change in the percent contribution of the OA factors to the total OA mass at the three sites. A large variation in OA composition was found with OOA dominating (>50%) between 10 am to 6 pm with a maximum value of ~70–80% during the afternoon hours indicating photochemical oxidation to be a major factor in the formation of OOA. OOA variation through the day was more or less similar between three sites indicating similarity in their formation pathways. POA contribution was >50% from late evening till early morning at all sites. These findings are consistent with an earlier study on PM$_1$ OA source apportionment using ACSM at IITD site (Bhandari et al., 2020), who reported POA (mostly retrieved as one mixed factor) dominating during the night (>50% contribution to total OA), whereas one secondary OA factor (OOA) factor dominating in the afternoon hours (up to 80% OA contribution). Among POA, SFC was more dominant at IITMDD and MRIIRS, having an average fractional contribution of 34% and 37% to total OA, and reaching up to ~60% and ~40% at midnight, respectively, indicating solid fuel combustion to be the major primary OA at these two sites during the evening and night hours, whereas, average SFC contribution was 25% at IITD. HOA was more dominant at IITD contributing on average 25% followed by IITMDD (21%) and MRIIRS (10%). Fractional HOA contribution at IITD varied significantly from 40% at midnight to less than 10% during the afternoon, whereas relatively stable at IITMDD (20–30%) and MRIIRS (<20%). Overall, the IITD site was more affected by traffic emissions, whereas IITMDD and MRIIRS from SFC emissions.

4. Conclusions

We measured highly time-resolved fine particulate matter concentrations and chemical composition in real-time at two urban sites (IITD and IITMDD) and one urban downwind site (MRIIRS) in the Delhi-NCR during the late winter period of 2018, using three aerosol mass spectrometers for non-refractory fraction, two aethalometers and one single particle soot photometer for refractory black carbon. Campaign mean PM$_{2.5}$ (eq.) at IITD and IITMDD (urban sites) were 153.8 ± 109.4 μg.m^{-3} and 127.8 ± 83.2 μg.m^{-3}, respectively, with average daily mean exceeding the WHO standard by 500% and 400%, respectively during the campaign period. PM$_1$ (eq.) at urban downwind site (MRIIRS) was 72.3 ± 44.0 μg.m^{-3}. Particles were composed of mainly organics (43–47%) followed by chloride (11–17%), ammonium (9–13%), sulfate (8–13%), nitrate (9–11%) and (5–16%) black carbon. Surprisingly high chloride concentration was observed during the morning hours with an hourly average concentration in PM$_{2.5}$ reaching up to 209.5 μg.m^{-3} and 126.4 μg.m^{-3} at IITD and IITMDD, respectively, while 68.2 μg.m^{-3} in PM$_1$ at MRIIRS.

OA source apportionment of highly mass-resolved data using ME-2 resulted in three primary factors including one traffic-related (HOA), two related to solid-fuel combustion (SFC-1 and SFC-2) and three secondary factors including two freshly oxidized factors (SVOOA-1 and SVOOA-2) and one highly oxidized factor (LVOOA), at IITD and MRIIRS sites. Whereas, unit mass resolution OA data at IITMDD was factorized into two primary factors (HOA and SFC) and one secondary factor (OOA). SFC-1 was influenced more by a mixture of coal-burning used for residential heating and burning of roadside trash including leaves, compostable waste, etc., whereas SFC-2 was probably affected by wood-burning emissions. While SFC at IITMDD was probably affected by a combination of SFC-1 and SFC-2 sources. SVOOA-1 and SVOOA-2 had significant differences in their mass spectra suggesting it be formed from different precursor compounds, with SVOOA-1 affected more from the oxidation of primary emissions rich in aromatic content, whereas SVOOA-2, by the oxidation of solid-fuel burning emissions.

Traffic-related emissions were more dominant at the IITD site with an average fractional contribution to the total OA mass reaching up to ~40 at midnight, whereas solid-fuel burning emissions were more dominating at IITMDD and MRIIRS with an average fractional contribution of

~40% and ~60% at midnight, respectively. OOA was the major contributor to the total OA mass with an average relative contribution of (45–55)% and reaching up to ~(70–80)% during the afternoon hours. Time series of total SOA estimated at the three sites were reasonably correlated (R^2 = 0.36–0.54), however, significant differences were observed in the absolute concentration levels between the two urban sites, indicating the influence of local emissions on total OOA concentration. Relatively similar PM chemical composition, diurnal and temporal variations between the three sites suggest similar type of sources affecting the particulate pollution in Delhi and adjoining cities, but variability in mass concentration suggest more local influence than regional.

CRediT authorship contribution statement

Vipul Lalchandani: Methodology, Software, Validation, Formal analysis, Investigation, Writing – original draft, Writing – review & editing, Visualization. **Varun Kumar:** Methodology, Software, Validation, Formal analysis, Investigation, Writing – review & editing. **Anna Tobler:** Methodology, Software, Validation, Formal analysis, Investigation, Writing – review & editing. **Navaneeth M. Thamban:** Investigation, Writing – review & editing. **Suneeti Mishra:** Investigation, Writing – review & editing. **Jay G. Slowik:** Methodology, Investigation, Writing – review & editing. **Deepika Bhattu:** Methodology, Investigation, Writing – review & editing. **Pragati Rai:** Investigation, Writing – review & editing. **Rangu Satish:** Investigation, Writing – review & editing. **Dilip Ganguly:** Resources, Writing – review & editing. **Suresh Tiwari:** Resources, Writing – review & editing. **Neeraj Rastogi:** Resources, Writing – review & editing. **Shashi Tiwari:** Resources, Writing – review & editing. **Griša Močnik:** Investigation, Writing – review & editing. **Andre S.H. Prévôt:** Writing – review & editing, Supervision, Project administration, Funding acquisition. **Sachchida N. Tripathi:** Writing – review & editing, Supervision, Project administration, Funding acquisition.

Declaration of competing interest

The authors declare that they have no known competing financial interests or personal relationships that could have appeared to influence the work reported in this paper.

Acknowledgement

Appendix A. Supplementary data

Supplementary data to this article can be found online at https://doi.org/10.1016/j.scitotenv.2021.145324.

References

Aiken, A.C., Decarlo, P.F., Kroll, J.H., Worsnop, D.R., Huffman, J.A., Docherty, K.S., Ulbrich, I.M., Mohr, C., Kimmel, J.R., Sueper, D., Sun, Y., Zhang, Q., Trimborn, A., Northway, M., Ziemann, P.J., Canagaratna, M.R., Onasch, T.B., Alfarra, M.R., Prevot, A.S.H., Dommen, J., Duplissy, J., Metzger, A., Baltensperger, U., Jimenez, J.L., 2008. O/C and OM/OC ratios of primary, secondary, and ambient organic aerosols with high-

resolution time-of-flight aerosol mass spectrometry. Environ. Sci. Technol. https://doi.org/10.1021/es703009q.

Albrecht, B.A., 1989. Aerosols, cloud microphysics, and fractional cloudiness. Science (80-.). doi:https://doi.org/10.1126/science.245.4923.1227.

Alfarra, M.R., Prevot, A.S.H. Szidat, S., Sandradewi, J., Weimer, S., Lanz, V.A., Schreiber, D., Mohr, M., Baltensperger, U., 2007. Identification of the mass spectral signature of organic aerosols from wood burning emissions. Environ. Sci. Technol. https://doi.org/10.1021/es062289b.

Allan, J.D., Delia, A.E., Coe, H., Bower, K.N., Alfarra, M.R., Jimenez, J.L., Middlebrook, A.M., Drewnick, F., Onasch, T.B., Canagaratna, M.R., Jayne, J.T., Worsnop, D.R., 2004. A generalised method for the extraction of chemically resolved mass spectra from aerodyne aerosol mass spectrometer data. J. Aerosol Sci. https://doi.org/10.1016/j.jaerosci.2004.02.007.

Bhandari, S., Gani, S., Patel, K., Wang, D.S., Soni, P., Arub, Z., Habib, G., Apte, J.S., Hildebrandt Ruiz, L., 2020. Sources and atmospheric dynamics of organic aerosol in New Delhi, India: insights from receptor modeling. Atmos. Chem. Phys. https://doi.org/10.5194/acp-20-735-2020.

Canagaratna, M.R., Jayne, J.T., Jimenez, J.L., Allan, J.D., Alfarra, M.R., Zhang, Q., Onasch, T.B., Drewnick, F., Coe, H., Middlebrook, A., Delia, A., Williams, L.R., Trimborn, A.M., Northway, M.J., DeCarlo, P.F., Kolb, C.E., Davidovits, P., Worsnop, D.R., 2007. Chemical and microphysical characterization of ambient aerosols with the aerodyne aerosol mass spectrometer. Mass Spectrom. Rev. https://doi.org/10.1002/mas.20115.

Canonaco, F., Crippa, M., Slowik, J.G., Baltensperger, U., Prévôt, A.S.H., 2013. SoFi, an IGOR-based interface for the efficient use of the generalized multilinear engine (ME-2) for the source apportionment: ME-2 application to aerosol mass spectrometer data. Atmos. Meas. Tech. https://doi.org/10.5194/amt-6-3649-2013.

Canonaco, F., Slowik, J.G., Baltensperger, U., Prévôt, A.S.H., 2015. Seasonal differences in oxygenated organic aerosol composition: implications for emissions sources and factor analysis. Atmos. Chem. Phys. https://doi.org/10.5194/acp-15-6993-2015.

Chakraborty, A., Bhattu, D., Gupta, T., Tripathi, S.N., Canagaratna, M.R., 2015. Real-time measurements of ambient aerosols in a polluted Indian city: sources, characteristics, and processing of organic aerosols during foggy and nonfoggy periods. J. Geophys. Res. https://doi.org/10.1002/2015JD023419.

Chakraborty, A., Tripathi, S.N., Gupta, T., 2017. Effects of organic aerosol loading and fog processing on organic aerosol volatility. J. Aerosol Sci. https://doi.org/10.1016/j.jaerosci.2016.11.015.

Cohen, A.J., Brauer, M., Burnett, R., Anderson, H.R., Frostad, J., Estep, K., Balakrishnan, K., Brunekreef, B., Dandona, L., Dandona, R., Feigin, V., Freedman, G., Hubbell, B., Jobling, A., Kan, H., Knibbs, L., Liu, Y., Martin, R., Morawska, L., Pope, C.A., Shin, H., Straif, K., Shaddick, G., Thomas, M., van Dingenen, R., van Donkelaar, A., Vos, T., Murray, C.J.L., Forouzanfar, M.H., 2017. Estimates and 25-year trends of the global burden of disease attributable to ambient air pollution: an analysis of data from the Global Burden of Diseases Study 2015. Lancet. https://doi.org/10.1016/S0140-6736(17)30505-6.

Crippa, M., Decarlo, P.F., Slowik, J.G., Mohr, C., Heringa, M.F., Chirico, R., Poulain, L., Freutel, F., Sciare, J., Cozic, J., Di Marco, C.F., Elsasser, M., Nicolas, J.B., Marchand, N., Abidi, E., Wiedensohler, A., Drewnick, F., Schneider, J., Borrmann, S., Nemitz, E., Zimmermann, R., Jaffrezo, J.L., Prévôt, A.S.H., Baltensperger, U., 2013a. Wintertime aerosol chemical composition and source apportionment of the organic fraction in the metropolitan area of Paris. Atmos. Chem. Phys. 13, 961–981. https://doi.org/10.5194/acp-13-961-2013.

Crippa, Monica, El Haddad, I., Slowik, J.G., Decarlo, P.F., Mohr, C., Heringa, M.F., Chirico, R., Marchand, N., Sciare, J., Baltensperger, U., Prévôt, A.S.H., 2013b. Identification of marine and continental aerosol sources in Paris using high resolution aerosol mass spectrometry. J. Geophys. Res. Atmos. https://doi.org/10.1002/jgrd.50151.

Crippa, M., Canonaco, F., Lanz, V.A., Äijälä, M., Allan, J.D., Carbone, S., Capes, G., Ceburnis, D., Dall'Osto, M., Day, D.A., DeCarlo, P.F., Ehn, M., Eriksson, A., Freney, E., Ruiz, L.H., Hillamo, R., Jimenez, J.L., Junninen, H., Kiendler-Scharr, A., Kortelainen, A.M., Kulmala, M., Laaksonen, A., Mensah, A.A., Mohr, C., Nemitz, E., O'Dowd, C., Ovadnevaite, J., Pandis, S.N., Petäjä, T., Poulain, L., Saarikoski, S., Sellegri, K., Swietlicki, E., Tiitta, P., Worsnop, D.R., Baltensperger, U., Prévôt, A.S.H., 2014. Organic aerosol components derived from 25 AMS data sets across Europe using a consistent ME-2 based source apportionment approach. Atmos. Chem. Phys. https://doi.org/10.5194/acp-14-6159-2014.

Dall'Osto, M., Ovadnevaite, J., Ceburnis, D., Martin, D., Healy, R.M., O'Connor, I.P., Kourtchev, I., Sodeau, J.R., Wenger, J.C., O'Dowd, C., 2013. Characterization of urban aerosol in Cork city (Ireland) using aerosol mass spectrometry. Atmos. Chem. Phys. https://doi.org/10.5194/acp-13-4997-2013.

DeCarlo, P.F., Kimmel, J.R., Trimborn, A., Northway, M.J., Jayne, J.T., Aiken, A.C., Gonin, M., Fuhrer, K., Horvath, T., Docherty, K.S., Worsnop, D.R., Jimenez, J.L., 2006. Field-deployable, high-resolution, time-of-flight aerosol mass spectrometer. Anal. Chem. https://doi.org/10.1021/ac061249n.

Draxler, R., Stunder, B., Rolph, G., Stein, A., Taylor, A., 2018. HYSPLIT4 User's Guide: Version 4.

Drinovec, L., Močnik, G., Zotter, P., Prévôt, A.S.H., Ruckstuhl, C., Coz, E., Rupakheti, M., Sciare, J., Müller, T., Wiedensohler, A., Hansen, A.D.A., 2015. The "dual-spot" aethalometer: an improved measurement of aerosol black carbon with real-time loading compensation. Atmos. Meas. Tech. https://doi.org/10.5194/amt-8-1965-2015.

Drinovec, L., Gregoric, A., Zotter, P., Wolf, R., Anne Bruns, E., Bruns, E.A., Prevot, A.S.H., Favez, O., Sciare, J., Arnold, I.J., Chakrabarty, R.K., Moosmüller, H., Filep, A., Mocnik, G., 2017. The filter-loading effect by ambient aerosols in filter absorption photometers depends on the coating of the sampled particles. Atmos. Meas. Tech. https://doi.org/10.5194/amt-10-1043-2017.

Elser, M., Huang, R.J., Wolf, R., Slowik, J.G., Wang, Q., Canonaco, F., Li, G., Bozzetti, C., Daellenbach, K.R., Huang, Y., Zhang, R., Li, Z., Cao, J., Baltensperger, U., El-Haddad, I.,

André, P., 2016. New insights into PM2.5 chemical composition and sources in two major cities in China during extreme haze events using aerosol mass spectrometry. Atmos. Chem. Phys. doi:https://doi.org/10.5194/acp-16-3207-2016.

Freutel, F., Schneider, J., Drewnick, F., Von Der Weiden-Reinmüller, S.L., Crippa, M., Prévôt, A.S.H., Baltensperger, U., Poulain, L., Wiedensohler, A., Sciare, J., Sarda-Estève, R., Burkhart, J.F., Eckhardt, S., Stohl, A., Gros, V., Colomb, A., Michoud, V., Doussin, J.F., Borbon, A., Haeffelin, M., Morille, Y., Beekmann, M., Borrmann, S., 2013. Aerosol particle measurements at three stationary sites in the megacity of Paris during summer 2009: meteorology and air mass origin dominate aerosol particle composition and size distribution. Atmos. Chem. Phys. https://doi.org/10.5194/acp-13-933-2013.

Fröhlich, R., Cubison, M.J., Slowik, J.G., Bukowiecki, N., Prévôt, A.S.H., Baltensperger, U., Schneider, J., Kimmel, J.R., Gonin, M., Rohner, U., Worsnop, D.R., Jayne, J.T., 2013. The ToF-ACSM: a portable aerosol chemical speciation monitor with TOFMS detection. Atmos. Meas. Tech. https://doi.org/10.5194/amt-6-3225-2013.

Fuzzi, S., Andreae, M.O., Huebert, B.J., Kulmala, M., Bond, T.C., Boy, M., Doherty, S.J., Guenther, A., Kanakidou, M., Kawamura, K., Kerminen, V.M., Lohmann, U., Russell, L.M., Pöschl, U., 2006. Critical assessment of the current state of scientific knowledge, terminology, and research needs concerning the role of organic aerosols in the atmosphere, climate, and global change. Atmos. Chem. Phys. https://doi.org/10.5194/acp-6-2017-2006.

Gani, S., Bhandari, S., Seraj, S., Wang, D.S., Patel, K., Soni, P., Arub, Z., Habib, G., Hildebrandt Ruiz, L., Apte, J.S., 2019. Submicron aerosol composition in the world's most polluted megacity: the Delhi aerosol supersite study. Atmos. Chem. Phys. 19, 6843–6859. https://doi.org/10.5194/acp-19-6843-2019.

Gao, R.S., Schwarz, J.P., Kelly, K.K, Fahey, D.W., Watts, L.A., Thompson, T.L., Spackman, J.R., Slowik, J.G., Cross, E.S., Han, J.H., Davidovits, P., Onasch, T.B., Worsnop, D.R., 2007. A novel method for estimating light-scattering properties of soot aerosols using a modified single-particle soot photometer. Aerosol Sci. Technol. https://doi.org/10.1080/02786820601118398.

Hallquist, M., Wenger, J.C., Baltensperger, U., Rudich, Y., Simpson, D., Claeys, M., Dommen, J., Donahue, N.M., George, C., Goldstein, A.H., Hamilton, J.F., Herrmann, H., Hoffmann, T., Iinuma, Y., Jang, M., Jenkin, M.E., Jimenez, J.L., Kiendler-Scharr, A., Maenhaut, W., McFiggans, G., Mentel, T.F., Monod, A., Prévôt, A.S.H., Seinfeld, J.H., Surratt, J.D., Szmigielski, R., Wildt, J., 2009. The formation, properties and impact of secondary organic aerosol: current and emerging issues. Atmos. Chem. Phys. https://doi.org/10.5194/acp-9-5155-2009.

Han, Z., Xie, Z., Wang, G., Zhang, R., Tao, J., 2016. Modeling organic aerosols over east China using a volatility basis-set approach with aging mechanism in a regional air quality model. Atmos. Environ. https://doi.org/10.1016/j.atmosenv.2015.05.045.

He, L.Y., Lin, Y., Huang, X.F., Guo, S., Xue, L., Su, Q., Hu, M., Luan, S.J., Zhang, Y.H., 2010. Characterization of high-resolution aerosol mass spectra of primary organic aerosol emissions from Chinese cooking and biomass burning. Atmos. Chem. Phys. 10, 11535–11543. https://doi.org/10.5194/acp-10-11535-2010.

Hu, M., Peng, J., Sun, K., Yue, D., Guo, S., Wiedensohler, A., Wu, Z., 2012. Estimation of size-resolved ambient particle density based on the measurement of aerosol number, mass, and chemical size distributions in the winter in Beijing. Environ. Sci. Technol. https://doi.org/10.1021/es204073t.

Jayne, J.T., Leard, D.C., Zhang, X., Davidovits, P., Smith, K.A., Kolb, C.E., Worsnop, D.R., 2000. Development of an aerosol mass spectrometer for size and composition analysis of submicron particles. Aerosol Sci. Technol. https://doi.org/10.1080/027868200410840.

Jimenez, J.L., Canagaratna, M.R., Donahue, N.M., Prevot, A.S.H., Zhang, Q., Kroll, J.H., DeCarlo, P.F., Allan, J.D., Coe, H., Ng, N.L., Aiken, A.C., Docherty, K.S., Ulbrich, I.M., Grieshop, A.P., Robinson, A.L., Duplissy, J., Smith, J.D., Wilson, K.R., Lanz, V.A., Hueglin, C., Sun, Y.L., Tian, J., Laaksonen, A., Raatikainen, T., Rautiainen, J., Vaattovaara, P., Ehn, M., Kulmala, M., Tomlinson, J.M., Collins, D.R., Cubison, M.J., Dunlea, E.J., Huffman, J.A., Onasch, T.B., Alfarra, M.R., Williams, P.I., Bower, K., Kondo, Y., Schneider, J., Drewnick, F., Borrmann, S., Weimer, S., Demerjian, K., Salcedo, D., Cottrell, L., Griffin, R., Takami, A., Miyoshi, T., Hatakeyama, S., Shimono, A., Sun, J.Y., Zhang, Y.M., Dzepina, K., Kimmel, J.R., Sueper, D., Jayne, J.T., Herndon, S.C., Trimborn, A.M., Williams, L.R., Wood, E.C., Middlebrook, A.M., Kolb, C.E., Baltensperger, U., Worsnop, D.R., 2009. Evolution of organic aerosols in the atmosphere. Science (80-.). doi:https://doi.org/10.1126/science.1180353.

Kanakidou, M., Seinfeld, J.H., Pandis, S.N., Barnes, I., Dentener, F.J., Facchini, M.C., Van Dingenen, R., Ervens, B., Nenes, A., Nielsen, C.J., Swietlicki, E., Putaud, J.P., Balkanski, Y., Fuzzi, S., Horth, J., Moortgat, G.K., Winterhalter, R., Myhre, C.E.L., Tsigaridis, K., Vignati, E., Stephanou, E.G., Wilson, J., 2005. Organic aerosol and global climate modelling: a review. Atmos. Chem. Phys. https://doi.org/10.5194/acp-5-1053-2005.

Kirchstetter, T.W., Novakov, T., Hobbs, P.V., 2004. Evidence that the spectral dependence of light absorption by aerosols is affected by organic carbon. J. Geophys. Res. D Atmos. https://doi.org/10.1029/2004JD004999.

Kumar, B., Chakraborty, A., Tripathi, S.N., Bhattu, D., 2016. Highly time resolved chemical characterization of submicron organic aerosols at a polluted urban location. Environ Sci Process Impacts https://doi.org/10.1039/c6em00392c.

Laborde, M., Crippa, M., Tritscher, T., Jurányi, Z., Decarlo, P.F., Temime-Roussel, B., Marchand, N., Eckhardt, S., Stohl, A., Baltensperger, U., Prévôt, A.S.H., Weingartner, E., Gysel, M., 2013. Black carbon physical properties and mixing state in the European megacity Paris. Atmos. Chem. Phys. https://doi.org/10.5194/acp-13-5831-2013.

Lanz, V.A., Alfarra, M.R., Baltensperger, U., Buchmann, B., Hueglin, C., Prévôt, A.S.H., 2007. Source apportionment of submicron organic aerosols at an urban site by factor analytical modelling of aerosol mass spectra. Atmos. Chem. Phys. https://doi.org/10.5194/acp-7-1503-2007.

Lanz, V.A., Alfarra, M.R., Baltensperger, U., Buchmann, B., Hueglin, C., Szidat, S., Wehrli, M.N., Wacker, L., Weimer, S., Caseiro, A., Puxbaum, H., Prevot, A.S.H., 2008. Source attribution of submicron organic aerosols during wintertime inversions by advanced factor analysis of aerosol mass spectra. Environ. Sci. Technol. https://doi.org/10.1021/es0707207.

Lanz, V.A., Prévôt, A.S.H., Alfarra, M.R., Weimer, S., Mohr, C., Decarlo, P.F., Gianini, M.F.D., Hueglin, C., Schneider, J., Favez, O., D'Anna, B., George, C., Baltensperger, U., 2010. Characterization of aerosol chemical composition with aerosol mass spectrometry in Central Europe: an overview. Atmos. Chem. Phys. doi:https://doi.org/10.5194/acp-10-10453-2010.

Lewis, K., Arnott, W.P., Moosmüller, H., Wold, C.E., 2008. Strong spectral variation of biomass smoke light absorption and single scattering albedo observed with a novel dual-wavelength photoacoustic instrument. J. Geophys. Res. Atmos. https://doi.org/10.1029/2007JD009699.

Liu, D., Allan, J., Whitehead, J., Young, D., Flynn, M., Coe, H., McFiggans, G., Fleming, Z.L., Bandy, B., 2013. Ambient black carbon particle hygroscopic properties controlled by mixing state and composition. Atmos. Chem. Phys. https://doi.org/10.5194/acp-13-2015-2013.

Middlebrook, A.M., Bahreini, R., Jimenez, J.L., Canagaratna, M.R., 2012. Evaluation of composition-dependent collection efficiencies for the aerodyne aerosol mass spectrometer using field data. Aerosol Sci. Technol. https://doi.org/10.1080/02786826.2011.620041.

Mohr, C., Huffman, J.A., Cubison, M.J., Aiken, A.C., Docherty, K.S., Kimmel, J.R., Ulbrich, I.M., Hannigan, M., Jimenez, J.L., 2009. Characterization of primary organic aerosol emissions from meat cooking, trash burning, and motor vehicles with high-resolution aerosol mass spectrometry and comparison with ambient and chamber observations. Environ. Sci. Technol. https://doi.org/10.1021/es8011518.

Mohr, C., DeCarlo, P.F., Heringa, M.F., Chirico, R., Slowik, J.G., Richter, R., Reche, C., Alastuey, A., Querol, X., Seco, R., Peñuelas, J., Jiménez, J.L., Crippa, M., Zimmermann, R., Baltensperger, U., Prévôt, A.S.H., 2012. Identification and quantification of organic aerosol from cooking and other sources in Barcelona using aerosol mass spectrometer data. Atmos. Chem. Phys. doi:https://doi.org/10.5194/acp-12-1649-2012.

Moteki, N., Kondo, Y., 2007. Effects of mixing state on black carbon measurements by laser-induced incandescence. Aerosol Sci. Technol. https://doi.org/10.1080/02786820701199728.

Moteki, N., Kondo, Y., 2010. Dependence of laser-induced incandescence on physical properties of black carbon aerosols: measurements and theoretical interpretation. Aerosol Sci. Technol. https://doi.org/10.1080/02786826.2010.484450.

Mukherjee, S., Singla, V., Pandithurai, G., Safai, P.D., Meena, G.S., Dani, K.K., Anil Kumar, V., 2018. Seasonal variability in chemical composition and source apportionment of submicron aerosol over a high altitude site in Western Ghats, India. Atmos. Environ. 180, 79–92. https://doi.org/10.1016/J.ATMOSENV.2018.02.048.

Nagar, P.K., Singh, D., Sharma, M., Kumar, A., Aneja, V.P., George, M.P., Agarwal, N., Shukla, S.P., 2017. Characterization of PM2.5 in Delhi: role and impact of secondary aerosol, burning of biomass, and municipal solid waste and crustal matter. Environ. Sci. Pollut. Res. doi:https://doi.org/10.1007/s11356-017-0171-3.

Ng, N.L., Canagaratna, M.R., Zhang, Q., Jimenez, J.L., Tian, J., Ulbrich, I.M., Kroll, J.H., Docherty, K.S., Chhabra, P.S., Bahreini, R., Murphy, S.M., Seinfeld, J.H., Hildebrandt, L., Donahue, N.M., Decarlo, P.F., Lanz, V.A., Prévôt, A.S.H., Dinar, E., Rudich, Y., Worsnop, D.R., 2010. Organic aerosol components observed in Northern Hemispheric datasets from aerosol mass spectrometry. Atmos. Chem. Phys. https://doi.org/10.5194/acp-10-4625-2010.

Ng, N.L., Herndon, S.C., Trimborn, A., Canagaratna, M.R., Croteau, P.L., Onasch, T.B., Sueper, D., Worsnop, D.R., Zhang, Q., Sun, Y.L., Jayne, J.T., 2011. An aerosol chemical speciation monitor (ACSM) for routine monitoring of the composition and mass concentrations of ambient aerosol. Aerosol Sci. Technol. https://doi.org/10.1080/02786826.2011.560211.

Paatero, P., 1999. The multilinear engine—a table-driven, least squares program for solving multilinear problems, including the n-way parallel factor analysis model. J. Comput. Graph. Stat. https://doi.org/10.1080/10618600.1999.10474853.

Paatero, P., Hopke, P.K., 2003. Discarding or downweighting high-noise variables in factor analytic models, in: Analytica Chimica Acta. https://doi.org/10.1016/S0003-2670(02)01643-4.

Paatero, P., Hopke, P.K., 2009. Rotational tools for factor analytic models. J. Chemom. https://doi.org/10.1002/cem.1197.

Paatero, P., Tapper, U., 1994. Positive matrix factorization: a non-negative factor model with optimal utilization of error estimates of data values. Environmetrics. https://doi.org/10.1002/env.3170050203.

Pant, P., Shukla, A., Kohl, S.D., Chow, J.C., Watson, J.G., Harrison, R.M., 2015. Characterization of ambient PM2.5 at a pollution hotspot in New Delhi, India and inference of sources. Atmos. Environ. doi:https://doi.org/10.1016/j.atmosenv.2015.02.074.

Patil, R.S., Kumar, R., Menon, R., Shah, M.K., Sethi, V., 2013. Development of particulate matter speciation profiles for major sources in six cities in India. Atmos. Res. https://doi.org/10.1016/j.atmosres.2013.04.012.

Peck, J., Gonzalez, L.A., Williams, L.R., Xu, W., Croteau, P.L., Timko, M.T., Jayne, J.T., Worsnop, D.R., Miake-Lye, R.C., Smith, K.A., 2016. Development of an aerosol mass spectrometer lens system for PM2.5. Aerosol Sci. Technol. doi:https://doi.org/10.1080/02786826.2016.1190444.

Petit, J.E., Favez, O., Albinet, A., Canonaco, F., 2017. A user-friendly tool for comprehensive evaluation of the geographical origins of atmospheric pollution: wind and trajectory analyses. Environ. Model. Softw. https://doi.org/10.1016/j.envsoft.2016.11.022.

Pope, C.A., Dockery, D.W., 2006. Health effects of fine particulate air pollution: lines that connect. J. Air Waste Manag. Assoc. https://doi.org/10.1080/10473289.2006.10464485.

Rai, P., Furger, M., El Haddad, I., Kumar, V., Wang, L., Singh, A., Dixit, K., Bhattu, D., Petit, J.E., Ganguly, D., Rastogi, N., Baltensperger, U., Tripathi, S.N., Slowik, J.G., Prévôt, A.S.H., 2020. Real-time measurement and source apportionment of elements in Delhi's atmosphere. Sci. Total Environ. https://doi.org/10.1016/j.scitotenv.2020.140332.

Saleh, R., Hennigan, C.J., McMeeking, G.R., Chuang, W.K., Robinson, E.S., Coe, H., Donahue, N.M., Robinson, A.L., 2013. Absorptivity of brown carbon in fresh and photochemically aged biomass-burning emissions. Atmos. Chem. Phys. https://doi.org/10.5194/acp-13-7683-2013.

Sandradewi, J., Prévôt, A.S.H., Szidat, S., Perron, N., Alfarra, M.R., Lanz, V.A., Weingartner, E., Baltensperger, U.R.S., 2008. Using aerosol light abosrption measurements for the quantitative determination of wood burning and traffic emission contribution to particulate matter. Environ. Sci. Technol. https://doi.org/10.1021/es702253m.

Sarangi, B., Aggarwal, S.G., Sinha, D., Gupta, P.K., 2016. Aerosol effective density measurement using scanning mobility particle sizer and quartz crystal microbalance with the estimation of involved uncertainty. Atmos. Meas. Tech. https://doi.org/10.5194/amt-9-859-2016.

Schnaiter, M., Horvath, H., Möhler, O., Naumann, K.H., Saathoff, H., Schöck, O.W., 2003. UV-VIS-NIR spectral optical properties of soot and soot-containing aerosols. J. Aerosol Sci. https://doi.org/10.1016/S0021-8502(03)00361-6.

Schnaiter, M., Linke, C., Möhler, O., Naumann, K.H., Saathoff, H., Wagner, R., Schurath, U., Wehner, B., 2005. Absorption amplification of black carbon internally mixed with secondary organic aerosol. J. Geophys. Res. D Atmos. https://doi.org/10.1029/2005JD006046.

Schwarz, J.P., Gao, R.S., Fahey, D.W., Thomson, D.S., Watts, L.A., Wilson, J.C., Reeves, J.M., Darbeheshti, M., Baumgardner, D.G., Kok, G.L., Chung, S.H., Schulz, M., Hendricks, J., Lauer, A., Kärcher, B., Slowik, J.G., Rosenlof, K.H., Thompson, T.L., Langford, A.O., Loewenstein, M., Aikin, K.C., 2006. Single-particle measurements of midlatitude black carbon and light-scattering aerosols from the boundary layer to the lower stratosphere. J. Geophys. Res. Atmos. https://doi.org/10.1029/2006JD007076.

Seinfeld, J., Pankow, J., 2003. Organic atmospheric particulate material. Annu. Rev. Phys. Chem. 54, 121–140.

Shamjad, P.M., Tripathi, S.N., Thamban, N.M., Vreeland, H., 2016. Refractive index and absorption attribution of highly absorbing brown carbon aerosols from an urban Indian city-Kanpur. Sci. Rep. https://doi.org/10.1038/srep37735.

Sharma, S.K., Mandal, T.K., Jain, S., Saraswati, Sharma, A., Saxena, M., 2016. Source apportionment of PM2.5 in Delhi, India using PMF model. Bull. Environ. Contam. Toxicol. https://doi.org/10.1007/s00128-016-1836-1.

Simoneit, B.R.T., Schauer, J.J., Nolte, C.G., Oros, D.R., Elias, V.O., Fraser, M.P., Rogge, W.F., Cass, G.R., 1999. Levoglucosan, a tracer for cellulose in biomass burning and atmospheric particles. Atmos. Environ. https://doi.org/10.1016/S1352-2310(98)00145-9.

Singhai, A., Habib, G., Raman, R.S., Gupta, T., 2017. Chemical characterization of PM1.0 aerosol in Delhi and source apportionment using positive matrix factorization. Environ. Sci. Pollut. Res. doi:https://doi.org/10.1007/s11356-016-7708-8.

Stein, A.F., Draxler, R.R., Rolph, G.D., Stunder, B.J.B., Cohen, M.D., Ngan, F., 2015. NOAA'S hysplit atmospheric transport and dispersion modeling system. Bull. Am. Meteorol. Soc. https://doi.org/10.1175/BAMS-D-14-00110.1.

Stephens, M., Turner, N., Sandberg, J., 2003. Particle identification by laser-induced incandescence in a solid-state laser cavity. Appl. Opt. https://doi.org/10.1364/ao.42.003726.

Subramanian, R., Kok, G.L., Baumgardner, D., Clarke, A., Shinozuka, Y., Campos, T.L., Heizer, C.G., Stephens, B.B., De Foy, B., Voss, P.B., Zaveri, R.A., 2010. Black carbon over Mexico: the effect of atmospheric transport on mixing state, mass absorption cross-section, and BC/CO ratios. Atmos. Chem. Phys. 10, 219–237. https://doi.org/10.5194/acp-10-219-2010.

Thamban, N.M., Tripathi, S.N., Moosakutty, S.P., Kuntamukkala, P., Kanawade, V.P., 2017. Internally mixed black carbon in the Indo-Gangetic Plain and its effect on absorption enhancement. Atmos. Res. 197, 211–223. https://doi.org/10.1016/j.atmosres.2017.07.007.

Thamban, N.M., Joshi, B., Tripathi, S.N., Sueper, D., Canagaratna, M.R., Moosakutty, S.P., Satish, R., Rastogi, N., 2019. Evolution of aerosol size and composition in the Indo-Gangetic Plain: size-resolved analysis of high-resolution aerosol mass spectra. ACS Earth Sp. Chem. 3, 823–832. https://doi.org/10.1021/acsearthspacechem.8b00207.

Tobler, A., Bhattu, D., Canonaco, F., Lalchandani, V., Shukla, A., Thamban, N.M., Mishra, S., Srivastava, A.K., Bisht, D.S., Tiwari, S., Singh, S., Močnik, G., Baltensperger, U., Tripathi, S.N., Slowik, J.G., Prévôt, A.S.H., 2020. Chemical characterization of PM2.5 and source apportionment of organic aerosol in New Delhi, India. Sci. Total Environ. 745, 1–12. https://doi.org/10.1016/j.scitotenv.2020.140924.

TWOMEY, S.A., PIEPGRASS, M., WOLFE, T.L., 1984. An assessment of the impact of pollution on global cloud albedo. Tellus B. https://doi.org/10.1111/j.1600-0889.1984.tb00254.x.

Ulbrich, I.M., Canagaratna, M.R., Zhang, Q., Worsnop, D.R., Jimenez, J.L., 2009. Interpretation of organic components from positive matrix factorization of aerosol mass spectrometric data. Atmos. Chem. Phys. https://doi.org/10.5194/acp-9-2891-2009.

Wang, Q., Huang, R.J., Cao, J., Han, Y., Wang, G., Li, G., Wang, Y., Dai, W., Zhang, R., Zhou, Y., 2014. Mixing state of black carbon aerosol in a heavily polluted urban area of China: implications for light absorption enhancement. Aerosol Sci. Technol. https://doi.org/10.1080/02786826.2014.917758.

Wang, J., Slowik, J., Tripathi, M., Bhattu, D., Rai, P., Kumar, V., Vats, P., Satish, R., Baltensperger, U., Ganguly, D., Rastogi, N., Sahu, L., Tripathi, S., Prévôt, A.S., 2020. Source characterization of volatile organic compounds measured by PTR-ToF-MS in Delhi, India. Atmos. Chem. Phys. Discuss. 1–27. https://doi.org/10.5194/acp-2020-11.

World Health Organisation, 2018. WHO Global Ambient Air Quality Database (Update 2018) [WWW Document]. Ambient Air Qual. Database (Update 2018).

Zhang, Q., Jimenez, J.L., Worsnop, D.R., Canagaratna, M., 2007. A case study of urban particle acidity and its influence on secondary organic aerosol. Environ. Sci. Technol. https://doi.org/10.1021/es061812j.

Zhang, Q., Jimenez, J.L., Canagaratna, M.R., Ulbrich, I.M., Ng, N.L., Worsnop, D.R., Sun, Y., 2011. Understanding atmospheric organic aerosols via factor analysis of aerosol mass spectrometry: a review. Anal. Bioanal. Chem. https://doi.org/10.1007/s00216-011-5355-y.

Zotter, P., Herich, H., Gysel, M., El-Haddad, I., Zhang, Y., Mocnik, G., Hüglin, C., Baltensperger, U., Szidat, S., Prévôt, A.S.H., 2017. Evaluation of the absorption Ångström exponents for traffic and wood burning in the Aethalometer-based source apportionment using radiocarbon measurements of ambient aerosol. Atmos. Chem. Phys. https://doi.org/10.5194/acp-17-4229-2017.